

# Star Formation in CALIFA survey perturbed galaxies. I. Effects of Tidal Interactions

A. Morales-Vargas,<sup>1\*</sup> J. P. Torres-Papaqui,<sup>1</sup> F. F. Rosales-Ortega,<sup>2</sup> S. F. Sánchez,<sup>3</sup>  
M. Chow-Martínez,<sup>4</sup> R. A. Ortega-Minakata,<sup>5</sup> J. J. Trejo-Alonso,<sup>6</sup>  
A. C. Robleto-Orús,<sup>1</sup> F. J. Romero-Cruz,<sup>7</sup> D. M. Neri-Larios<sup>8</sup>  
& the CALIFA survey Collaboration<sup>9</sup>

<sup>1</sup>Departamento de Astronomía, Universidad de Guanajuato, Apartado Postal 144, Guanajuato 36000, Mexico

<sup>2</sup>Instituto Nacional de Astrofísica, Óptica y Electrónica, Luis Enrique Erro 1, Tonantzintla 72840, Mexico

<sup>3</sup>Instituto de Astronomía, Universidad Nacional Autónoma de México (UNAM), Apartado Postal 70-264, México D. F. 04510, Mexico

<sup>4</sup>Instituto de Geología y Geofísica, Universidad Nacional Autónoma de Nicaragua, Rotonda Universitaria

Rigoberto López Pérez 150 metros al Este, Managua 663, Nicaragua

<sup>5</sup>Instituto de Radioastronomía y Astrofísica (IRyA), UNAM, Apartado Postal 72-3, Morelia, Michoacán 58089, Mexico.

<sup>6</sup>Facultad de Ingeniería, Universidad Autónoma de Querétaro, Cerro de las Campanas s/n, Centro Universitario,

Santiago de Querétaro 76010, Mexico

<sup>7</sup>Instituto Tecnológico Superior de Guanajuato, Guanajuato 36262, Mexico

<sup>8</sup>School of Physics, The University of Melbourne, Parkville, VIC. 3010, Australia

<sup>9</sup><https://califa.caha.es/>

Accepted XXX. Received YYY; in original form ZZZ

## ABSTRACT

We explore the effects of tidal interactions on star formation (SF) by analysing a sample of CALIFA survey galaxies. The sample consists of tidally and non-tidally perturbed galaxies, paired at the closest stellar mass densities for the same galaxy type between subsamples. They are then compared, both on the resolved Star Formation Main Sequence (SFMS) plane and in annular property profiles. Star-forming regions in tidally perturbed galaxies exhibit flatter SFMS slopes compared to star-forming regions in non-tidally perturbed galaxies. Despite that the annular profiles show star-forming regions in tidally perturbed galaxies as being mostly older, their SF properties are never reduced against those ones proper of non-tidally perturbed galaxies. Star-forming regions in non-tidally perturbed galaxies are better candidates for SF suppression (quenching). The lowered SF with increasing stellar mass density in tidally perturbed galaxies may suggest a lower dependence of SF on stellar mass. Though the SFMS slopes, either flatter or steeper, are found independent of stellar mass density, the effect of global stellar mass can not be ignored when distinguishing among galaxy types. Since a phenomenon or property other than local/global stellar mass may be taking part in the modulation of SF, the integrated SF properties are related to the tidal perturbation parameter. We find weak, but detectable, positive correlations for perturbed galaxies suggesting that tidal perturbations induced by close companions increase the gas accretion rates of these objects.

**Key words:** galaxies: evolution – galaxies: interactions – galaxies: star formation

## 1 INTRODUCTION

Characterizing the unlike or opposite natures of *passive* and *forced* galaxy evolution via *quiescent* and *induced*

star formation (SF) has been vastly intriguing. Interactions are, undoubtedly, typical *actuators* of SF. In galaxy *mergers* and *pairs*, gravitational tidal effects use to induce SF by overrunning the self-gravity of the progenitors (*e.g.* Barnes & Hernquist 1991, 1996; Freedman Woods & Geller 2007).

In galaxy mergers, enhanced conversions of both molec-

\* E-mail: abdmoralesv@gmail.com (AM)

ular and atomic gas may yield SF efficiencies of at least one order of magnitude larger (*e.g.* Mihos, Richstone & Bothun 1992; Beck & Kovo 1994; Mihos & Hernquist 1994, 1996; Young 1999; Li *et al.* 2008). For these cases, simulating the response of global SF is complex: it depends on orbital dynamics, aligned disk spin orientations of the progenitors, their gas fraction and distribution, mass ratios (*e.g.* Mihos, Richstone & Bothun 1992; Mihos & Hernquist 1996; Tissera *et al.* 2002; Bergvall, Laurikainen & Aalto 2003; Cox 2004; Perez *et al.* 2005; Davies *et al.* 2015); as well as models for prescribing SF and feedback (*e.g.* Springel 2000; Barnes 2004; Springel, Di Matteo & Hernquist 2005; Hopkins *et al.* 2013). Whereas the lower-mass (secondary) galaxy in *minor* mergers appears to be the most affected by the interaction (*e.g.* Alonso-Herrero *et al.* 2012 and references therein), both galaxies in *major* mergers use to suffer of enhanced SF (*e.g.* Mastropietro *et al.* 2005; Freedman Woods & Geller 2007; Davies *et al.* 2015; Moreno *et al.* 2015). Major mergers are relatively easy to identify whereas minor mergers, more frequent in the local Universe, may also contribute to drive galaxy evolution (Ventou *et al.* 2019 and references therein).

Though galaxy pairs also show molecular gas fraction enhancements due to tidal torques (*e.g.* Violino *et al.* 2018), passing-by encounters are less effective in triggering SF (*e.g.* Mihos, Richstone & Bothun 1992; Freedman Woods & Geller 2007). However, retrograde encounters of the flyby-passing disks may increase such that effectiveness (*e.g.* Wild *et al.* 2014). Not least in importance, the merger fraction and in general the build up of stellar mass greatly depend on the estimation of galaxy pairs (*e.g.* Yan-Chun *et al.* 2003; Keenan *et al.* 2013; Ventou *et al.* 2019).

Either hiked or weakly raised, most induced SF is centrally located (*e.g.* Hernquist & Mihos 1995; Mihos & Hernquist 1994, 1996; Springel 2000; Mayer *et al.* 2001; Yuan *et al.* 2012; Hopkins *et al.* 2013; Moreno *et al.* 2015; Argudo-Fernández *et al.* 2016). This may be due to gas inflows (*e.g.* Capelo *et al.* 2015; Blecha *et al.* 2018) though important amounts of gas are either ejected by winds (*e.g.* Hopkins *et al.* 2008; Wild *et al.* 2014; López-Cobá *et al.* 2017, 2018) or stripped off from galaxies (*e.g.* Di Matteo *et al.* 2008; Bitsakis *et al.* 2010). Since off-central SF is either hard to trigger or so short-lived, interactions prevail as activators of gas inflows.

Additionally, galaxy environment peculiarly affects SF. Measurements of compaction/expansion of a collection of objects within a certain limited phase space have been done so far (*e.g.* Lewis *et al.* 2002; Gómez *et al.* 2003; Kauffmann *et al.* 2004; Gavazzi *et al.* 2010; Calvi *et al.* 2011; Vulcani *et al.* 2015; Schaefer *et al.* 2017). Recently, Zheng *et al.* (2017) model the morphology of the local cosmic density field. Girregularard *et al.* (2017) split into centrals and satellites to compare Stellar Population (SP) gradients. Gavazzi *et al.* (2010) and Girregularard *et al.* (2017) particularly discuss the biases a local density parameter may yield. If appearing far from a main aggregate (*i.e.*, being an outlier in the velocity distribution) the density of an object would be lower than the true one, that if there were indeed significant gravitational interactions in the aggregate. If background/foreground objects not physically related to

the object and aggregate were present, evaluating the density of the former would be senseless.

Another concept in line with galaxy evolution is the so-called Star Formation Main Sequence (SFMS, *e.g.* Brinchmann *et al.* 2004; Elbaz *et al.* 2007; Salim *et al.* 2007; Peng *et al.* 2010; Whitaker *et al.* 2012; Speagle *et al.* 2014; Renzini & Peng 2015; Cano-Díaz *et al.* 2016; Erfanianfar *et al.* 2016; Catalán-Torrecilla *et al.* 2017; Ellison *et al.* 2018a; López-Fernández *et al.* 2018; Sánchez *et al.* 2018a; Medling *et al.* 2018; Erroz-Ferrer *et al.* 2019). From internal to external processes, it has been assisting to identify what modulates SF, specially, up to  $z \sim 1$ . Great debate however has emerged due to either its uncertainties (*e.g.* Elbaz *et al.* 2007; Peng *et al.* 2010), or the fact that it should not be considered a linear relation (Erfanianfar *et al.* 2016), mainly, at  $\log_{10} M_*(M_\odot) > 10$ . Certainly, a flat slope characterizes the SFMS for these masses (Whitaker *et al.* 2012; Erfanianfar *et al.* 2016), often related to bulge-dominated galaxies, what gives the sequence a large dispersion (Schiminovich *et al.* 2007; Salim *et al.* 2007; Whitaker *et al.* 2012; González-Delgado *et al.* 2016). A quite broad sequence for late type galaxies has even been reported due to the stochasticity of the star-forming regions (Vulcani *et al.* 2019).

If adapting a linear model, the SFMS logarithmic slope has resulted quite fluctuating (*e.g.* Elbaz *et al.* 2007; Speagle *et al.* 2014; Renzini & Peng 2015; Cano-Díaz *et al.* 2016; Maragkoudakis *et al.* 2017; Sánchez *et al.* 2018a). Speagle *et al.* (2014) show this is due to its dependence on time evolution and other not less important factors (Initial Mass Function, IMF; Star Formation Rate SFR tracers; SP models; etc.). By confirming this time dependency, López-Fernández *et al.* (2018) and Sánchez *et al.* (2018a) have unveiled the cosmic SF quenching not as simple as a one-event process since a fraction of high- $z$  passive galaxies have become rejuvenated at lower redshifts and ended quenched later on.

By featuring the SFR intensity ( $\Sigma_{\text{SFR}}$ ) and stellar mass surface density ( $\Sigma_*$ ) in a spatially-resolved SFMS, Cano-Díaz *et al.* (2016) and González-Delgado *et al.* (2016) predict a slightly steeper integrated (global) sequence. This appears to have its origin in the spatially-resolved sequence (Hsieh *et al.* 2017; Maragkoudakis *et al.* 2017; Cano-Díaz *et al.* 2019). Generally, the resolved SFMS assists to figure out how complex the regulation of SF is (external, global and local actuators, Medling *et al.* 2018). For instance, by integrating galaxy components, Catalán-Torrecilla *et al.* (2017) show massive disks as having undergone efficient SF suppression. Hsieh *et al.* (2017) find reduced fractions of H II regions from the periphery of quenched galaxies. Later, from SFMS offsets, Ellison *et al.* (2018a) show that SF enhancements/suppressions occur inside-out. Hall *et al.* (2018) find sequences with contrasting patterns which may result from the rate of mass inflows. Cano-Díaz *et al.* (2019) propose that local SF is indirectly modulated by galaxy morphology.

A pair of goals are introduced with all this background. To get insight on centrally driven/located gas/SF and their plausible relation with tidal interactions (*e.g.* Ellison *et al.* 2018b and references therein), we compare the  $\Sigma_{\text{SFR}}$  (SFR  $\text{kpc}^{-2}$ ) annular profiles of star-forming regions

within tidally and non-tidally perturbed galaxies. Instead of a local density measurement, we treat each tidally perturbed object by simply considering its closest neighbour. There is no distinction, for instance, if centrals or satellites, but just galaxies under tidal torques, neither in rigorous established pairs nor in groups nor in clusters. The quite challenging task of establishing a general characterization of environment justifies this approach since different estimations are relevant for different physical effects (Walcher *et al.* 2014).

Secondly, as close encounters use to unbalance SF, we look for a possible dependence of the resolved SFMS on unlike degrees of interaction. To do so, the star-forming regions within our non-tidally/tidally perturbed galaxies are pictured in the  $\Sigma_{\text{SFR}}-\Sigma_*$  plane.

For a good direction of both goals we use:

(i) Integral Field Spectroscopy (IFS), perfectly suitable to spatially split up detailed distributions of any property of concern. The Calar Alto Legacy Integral Field Area (CALIFA, Sánchez *et al.* 2012a; Husemann *et al.* 2013; García-Benito *et al.* 2015; Sánchez *et al.* 2016a) survey is used for this purpose. The CALIFA survey favorably presents the best compromise among near-by coverage ( $0.005 \leq z \leq 0.03$ ), spatial coverage (mostly to 2.5 effective radius), spatial resolution ( $\sim 1$  kpc), number of targets ( $> 600$ ) and target sampling ( $\sim 4,000$  spectra per target).

(ii) Synthesis of Stellar Populations (SSPs) by applying detailed spectral synthesis techniques (*e.g.* Cid Fernandes *et al.* 2005; Asari *et al.* 2007).

This paper is ordered as follows. Methods to obtain the SP properties are described in Section 2. Our samples are defined in Section 3. We present resolved SFMSs and our property profiles in Section 4. We discuss both results in Section 5. Summary and conclusions are stated in Section 6.

We use a cosmological set of  $H_0 = 72 h_{72}^{-1} \text{ km s}^{-1} \text{ Mpc}^{-1}$ ,  $\Omega_M = 0.3$  and  $\Omega_\Lambda = 0.7$ ; a Chabrier (2003) IMF for SFR and stellar mass ( $M_*$ ) estimations; and a 0.05 level of significance for all statistics.

## 2 METHODS

### 2.1 Stellar component subtraction and emission line fitting

One spectrum is contained in the third (wavelength) dimension of each spaxel<sup>1</sup>. These are extracted, read, and selected only those with at least one non-NULL value (typically  $\sim 4000$ , *i.e.*,  $\sim 78\%$  of a data cube<sup>2</sup>). Our processing pipeline rebins this selection to the resolution of the STARLIGHT code (SSPs, Cid Fernandes *et al.* 2005). The code version relies on the MILES base of spectral libraries (Sánchez-Blázquez *et al.* 2006; Falcón-Barroso *et al.* 2011) and uses the simple SPs of Bruzual & Charlot (2003) synthesis models (Chabrier 2003 IMF). STARLIGHT satisfactorily solves spectra with no NULLs along the wavelength dimension (typically  $\sim 3000$ , *i.e.*,  $\sim 60\%$  of a data cube). The

nearly pure nebular spectra, result from subtracting the stellar syntheses, are taken to fit the emission lines of interest by adapting Gaussian profiles. Central wavelength, amplitude and associated dispersion for each line are initial parameters. Iterations are done till finding the minimum  $\chi^2$  value (residual) between the observed line and the best profile. Isolated lines are fit individually whereas multiple profiles ( $G = G_1 + G_2 + \dots + G_n$ ) are constructed for blended lines. The signal-to-noise (S/N) at the observed central wavelength of each emission line serves to estimate flux uncertainties. Full width at half maximum (FWHM) and wavelength displacements are also estimated.

### 2.2 Galaxy morphologies and colours

The CALIFA survey Collaboration (hereafter “the Collaboration”) carried out a morphological re-classification for all galaxies of the CALIFA survey Mother Sample (MS, *i.e.*, the set of candidates for the survey observations, see Walcher *et al.* 2014, W-14 from now on). On Sloan Digital Sky Survey (SDSS) images ( $r$  and  $i$  bands), five collaborators based their respective visual classifications on the following: 1) E, S, or I for elliptical, spiral or irregular; 2) 0-7 for E; 0a, a, ab, b, bc, c, cd, d and m for S; or r for I; 3) B for barred, A for unbarred or AB if unsure; and 4) merger features, yes (Y) or no (N). The five classifications were combined to obtain each mean by ignoring outliers. Appendix A lists the resultant morphologies for the galaxies involved in this work.

Galaxy colours are determined from colour magnitude diagrams (CMDs) which use SDSS/DR7 (Abazajian *et al.* 2009) model magnitudes<sup>3</sup> (see Fig. 3). The Eqs. giving the cuts to select “red” and “blue” galaxies are:

$$g-r = -0.0371 \times (M_r + 24) + 0.81 \quad \text{and} \quad (1)$$

$$g-r = (-0.0371 \times (M_r + 24) + 0.81) - 0.12,$$

where  $M_r$  is the  $r$ -band absolute magnitude. Both Eqs. are within a 0.98 confidence interval and represent correlations for the “red sequence” and “blue cloud” respectively. We derive them by using Eqs. 1 and 2 of Schawinski *et al.* (2014) on data of all SDSS/DR7 objects. Finally, “green” galaxies are in-between cuts.

### 2.3 Star-forming regions, SFRs and stellar masses

#### 2.3.1 Star-forming regions, SFR & $\Sigma_{\text{SFR}}$ estimations

Prior to define the star-forming regions, the dominant source of gas excitation is determined. The Baldwin, Phillips & Terlevich (1981) diagram (BPT, their fig. 5) is the standard tool for this. Line demarcations used for pure star-forming galaxy (SFG) and active galactic nucleus (AGN) excitations are respectively those of Kauffmann *et al.* (2003a) and Kewley *et al.* (2001). In-between excitation is often dubbed as Transition Object

<sup>1</sup> An IFS discrete spatial element (Rosales-Ortega *et al.* 2010).

<sup>2</sup> This reflects the unavoidable fiber loss of throughput close to the edges and gradually increasing towards the corners of the instrument detector (Sánchez *et al.* 2012a).

<sup>3</sup> Model magnitudes are optimal measures of fluxes of galaxies. They result from fitting two galaxy models on each object in each band. The highest likelihood model in the  $r$  band (modelMag, <https://bit.ly/3e4wKm5>) is chosen and applied to the other bands after convolving with the point spread function in each band.

**Table 1.** Emission line and mass-and-age criteria (e.g. Cid Fernandes *et al.* 2007, 2010; Asari *et al.* 2007).

STARLIGHT S/N (continuum window: 5075–5125 Å)	Emission line flux ( $\times 10^{-16}$ ergs $^{-1}$ cm $^{-2}$ Å $^{-1}$ )	Observed emission line $\sigma$ (kms $^{-1}$ )	Emission line S/N	Line displacement $\lambda_{lab} - \lambda_{obs}$ (Å)
$\geq 5^a$	$1000 \geq \text{flux} \geq 0.1$	$< 400$	$\geq 3^b$	$< 10$
$\geq 10^c$	...	...	...	...

<sup>a</sup> Excitation sources and SFRs (Sections 2.3.1).

<sup>b</sup> Appropriate lower limit for H $\beta$  and [O III] $\lambda$ 5007 line detections (e.g. Cid Fernandes *et al.* 2010).

<sup>c</sup> Approximation of global stellar mass and SP median age (Section 2.3.2).

(TO). Torres-Papaqui *et al.* (2012b) demarcate Seyfert 2 (Sy2) excitation and Low Ionization (Nuclear) Emission line Regions (LI(N)ERs).

Our pipeline for analysis applies then the SFG spectral characterization of Cid Fernandes *et al.* (2007, 2010) and Asari *et al.* (2007). It requires that the four emission lines that construct the BPT diagram fulfill the line criteria of Table 1 (first-row). If a “resolved” BPT diagram can be extracted from a galaxy, this will be an Emission Line Galaxy (ELG) since both the H $\alpha$  and N [II] $\lambda$ 6583 lines have a S/N  $\geq 3$  (Cid Fernandes *et al.* 2010; Torres-Papaqui *et al.* 2012a). It is implicit, later in the text, the preference given to objects containing star-forming regions. Active objects like these are the cornerstone to portray galaxy evolution in terms of SP properties. To assign the dominant excitation source (see Table A1), the comparison of line ratios is done by previously integrating (summing up) all resolved fluxes of each involved line.

For star-forming regions, we proceed as follows. For all galaxy sets, the pipeline for analysis selects spectra which pass the full line criteria for H $\alpha$ , and only the flux criterion for the rest lines of the BPT. This is due to two facts: 1) the H $\alpha$  line emission is our SFR tracer, and 2) if all line criteria is applied on the rest lines, the [N II] one, mainly, reduces the number of star-forming regions, usually, in blue galaxies. Next, we truncate each set by using an EW cut-off. Besides of proving strong excitation, an EW (H $\alpha$ ) cut-off of  $\geq 6$  Å characterizes both, star-forming regions with [O II]-[O III] line S/N  $\geq 3$  (Cid Fernandes *et al.* 2010), and H II regions with big fractions of young SPs (Sánchez *et al.* 2014). This truncation by itself effectively omits spaxels of observation artefacts and those of foreground stars.

For the extinction of H $\alpha$  flux, the pipeline re-iterates, in each truncated set, the full line criteria on now the H $\beta$  line. Such that line mostly succeeds the criteria. For just several galaxies, failed spectra are a  $\sim 5\%$  or less. Extinction correction is not applied in these failed cases. We use an intrinsic Balmer ratio of 2.86 for Case B recombination at  $T_e = 10,000$  K and  $n_e = 100$  cm $^{-3}$  (Hummer & Storey 1987). We use equation 1 of Catalán-Torrecilla *et al.* (2015):

$$A(H\alpha) = \left[ \frac{K_{H\alpha}}{-0.40(K_{H\alpha} - K_{H\beta})} \right] \cdot \log_{10} \left[ \frac{F_{H\alpha}/F_{H\beta}}{2.86} \right], \quad (2)$$

where  $K_{H\alpha} = 2.54$  and  $K_{H\beta} = 3.61$  are the extinction coefficients from the Galaxy extinction curve (Cardelli, Clayton & Mathis 1989). If  $F_{H\alpha}/F_{H\beta} < 2.86$ , no extinction is assumed. The pipeline then takes each EW-

truncated, extinction-corrected set to assign excitation sources to each single region. Only those with SFG excitation are selected for the conversion of Asari *et al.* (2007):

$$\text{SFR} (\text{M}_{\odot} \text{yr}^{-1}) = 5.2 \times 10^{-42} L_{H\alpha} (\text{ergs}^{-1}), \quad (3)$$

which uses a Chabrier (2003) IMF (0.1–100  $\text{M}_{\odot}$ ) to ensure the most ionizing stars and a SF constancy of the order of their lifetime ( $\sim 10$  Myr). Notice then that, regardless of the dominant excitation source determined earlier, the star-forming regions are defined as those spaxels whose spectra show EW (H $\alpha$ )  $\geq 6$  Å and that lay below the Kauffmann *et al.* (2003a) demarcation in the BPT.

Global SFRs are the sum of SFRs of all star-forming regions. These resolved rates are indeed measurements of  $\Sigma_{\text{SFR}}$  (each spaxel has an angular surface of 1 arcsec $^2$ ). Obeying the Hubble flow, the distance to each galaxy is estimated and with it the correction factor for linear surface scale (kpc $^2$ , see Fig. 1 and Table A1).

### 2.3.2 Global stellar mass and median age

Total stellar masses and mean SP ages are extracted from the STARLIGHT output. The former are the current masses in stars whilst the latter are the mean light-weighted stellar ages according to Cid Fernandes *et al.* (2005, their equation 2). To estimate both global  $\text{M}_{\star}$  and SP median age for each galaxy, we use the S/N for a meaningful SP fit for integrated spectra (second-row criterion of Table 1, Cid Fernandes *et al.* 2010). Global  $\text{M}_{\star}$  is the sum of resolved contributions whilst SP median age is the median of the age distributions of all spaxels. In our spectral sets, the restriction of above effectively omits spurious spectra of background galaxies but not of foreground stars so these are manually masked. Likewise the SFR, the  $\text{M}_{\star}$  of each star-forming region is indeed a measurement of  $\Sigma_{\star}$ .

## 3 GALAXY SAMPLES

### 3.1 The tidal perturbation parameter

W-14 looked for neighbours of each CALIFA survey galaxy. In the SDSS/DR8 (Aihara *et al.* 2011), these neighbours are objects: 1) classified as galaxies, 2) within 200 kpc from the CALIFA survey targets, 3) with reliable values of Petrosian radii, 4) spanning sizes of at least 2 kpc, and 5) with good quality flags.

Once the neighbours are identified, W-14 calculate what we use as criterion of segregation, the tidal perturbation parameter ( $f$ , Byrd *et al.* 1986; Varela *et al.* 2004):

$$f = \log \left( \frac{F_{prim}}{F_{sec}} \right) = 3 \log \left( \frac{R}{b} \right) + 0.4 (m_{sec} - m_{prim}). \quad (4)$$

$F_{prim}$  indicates the tidal force exerted by the primary galaxy;  $F_{sec}$ , the internal force in the outskirts of the secondary;  $m_{prim}$  and  $m_{sec}$ , their respective apparent magnitudes;  $R$ , the secondary disk radius; and  $b$ , the perigalactic distance of the

<sup>4</sup> Mostly compact regions. Lacerda *et al.* 2018 prove that an EW (H $\alpha$ )  $> \sim 10$  Å distinguishes star-forming from diffuse ionized gas regions.

primary. Varela *et al.* (2004) discuss that only for very eccentric orbits and when the primary is around the apocentre  $f$  would fail in pointing true perturbed galaxies (also see Schaefer *et al.* 2019). They verify that errors of 20% in  $b$  and/or mass, result in errors of at most a few tenths in  $f$ . For equal primary and secondary galaxy masses,  $f \geq -2$  implies  $b$  close enough to clearly induce global instability (Byrd & Howard 1992). On the other hand, Varela *et al.* (2004) obtain the  $f$  distribution of the Coma cluster which shows no galaxies with  $f < -4.5$ . Assuming that an aggregate as rich as a cluster is not a place for a typical non-tidally-perturbed galaxy, they adopt this criterion for no perturbation (so that an  $f \geq -4.5$  implies tidal perturbation).

W-14 find  $f$  and the galaxy interaction state well correlated. The latter results from separated eye-classifications of SDSS images ( $r$  and  $i$  bands) within the Collaboration. They find  $f = -4.0$  ( $\sigma = 1.7$ ) for non-interacting galaxies and  $f = -2.9$  ( $\sigma = 2.0$ ) for interacting ones.

### 3.2 The observational strategy

The MS was selected from the SDSS/DR7 photometric catalogue to include all galaxies with an  $r$ -band isophotal diameter of  $45'' < d < 79.2''$  ( $0.005 < z < 0.03$ ). The selection of these candidates is mainly based on visibility and to fit the PMAS/PPak field-of-view (see W-14). The PMAS (Roth *et al.* 2005)/PPak (Kelz *et al.* 2006; Bershadsky *et al.* 2010) integral field spectrograph, mounted on the Calar Alto 3.5 m telescope, was used to perform the survey observations. Mostly all these were selected from the MS. A three dithering scheme was adopted to fill the gaps among PPak fibers. With this, the vignetting trouble and spatial resolution are respectively reduced and improved (Sánchez *et al.* 2012a). Two different but complementary set ups were used to perform all observations. The one of medium resolution is used here ( $\lambda/\Delta\lambda \sim 850$  at  $\sim 5000 \text{ \AA}$ , FWHM  $\sim 6 \text{ \AA}$ ). Its main purpose is to study the SPs and the properties of the ionized gas by including as much emission line species as possible (*i.e.*, the widest wavelength range, 3745-7300  $\text{\AA}$ ).

The improved spectrophotometric calibration and registering of the images are finally remarked. The scaling of the absolute flux levels of the datacubes to SDSS/DR7 broad-band photometry is better than a 15% (DR1, Husemann *et al.* 2013). Later, it improves to  $\sim 8\%$  due to a new registering procedure (DR2, DR3, García-Benito *et al.* 2015; Sánchez *et al.* 2016a). Predicted SDSS fluxes for the PPak fibers are compared with those of the spaxel spectra themselves at each pointing position. The photometric scale factor at the best matching position is used to rescale the absolute photometry of each particular pointing of the spectra. The reliability of the nebular fluxes is reinforced<sup>5</sup>. However, for irregular cases such as edge-on galaxies, the registering fails so the previous calibration is re-used.

<sup>5</sup> Aperture size corrections are even needless:  $\sim 97\%$  of CALIFA survey galaxies are covered out to at least  $2 \times$  the SDSS Petrosian half light radius as computed from the growth curve photometry (see Sánchez *et al.* 2016a).

### 3.3 The selection of the samples

The CALIFA survey consists of 667 objects<sup>6</sup>. From them, 542 are a subset of the MS. The fraction of 529 out of 542 was observed in the widest wavelength range. From it, 454 objects have  $f$  estimations (W-14). Under the criterion of Varela *et al.* (2004), *i.e.*  $f < -4.5$  for no perturbation, 101 are non-tidally perturbed and 353 are tidally perturbed.

We obtain the resolved BPT diagram, with a median star-forming region fraction of 0.85, for 62 out of the 101 non-tidally-perturbed objects (61%). Such 62 ones are then ELGs (see Section 2.3.1) and 41/62 of them are Late Type Spirals (LTSSs, see Table A1). The  $f$  parameter cumulative distribution function of the 62 objects is also nearly normal (see Fig. 1, bottom). This effective set of non-tidally perturbed objects is called hereafter the *control* sample. Similarly, we obtain the resolved BPT diagram, with 0.81 as the median fraction of star-forming regions, for 231 out of the 353 tidally-perturbed objects (65%). These are ELGs as well. To perform fair comparisons of SP properties, we construct from these perturbed ELGs, ten subsets with 62 objects each that mimic as close as possible five fundamental properties of the control sample. These properties are  $M_*$ , redshift ( $z$ ), morphological group, galaxy colour and the dominant excitation source (see Table A1). The reasons behind these fundamentals are the following.

- (i)  $M_*$  to control differences in SF records.
- (ii)  $z$  to minimize contrasts in spatial or surface scales and number of star-forming regions.
- (iii) Morphological group since morphology contributes (at least) to stabilize SF (*e.g.* Martig *et al.* 2009, Martig *et al.* 2013, González-Delgado *et al.* 2015, Cano-Díaz *et al.* 2019, Méndez-Abreu *et al.* 2019, Koyama *et al.* 2019).
- (iv) Galaxy colour for homogeneous photometry.
- (v) The dominant source of gas excitation to balance the influence of a plausible massive black hole (AGN feedback, *e.g.* Schawinski *et al.* 2007; Fabian 2012; Cicone *et al.* 2014).

From the 231 perturbed ELGs, the ten samples, trials A to J (62 objects each), are built in a two-step procedure. Trials A to E are obtained first sort ascending the control sample by  $M_*$ <sup>7</sup>. The most approximated case in the above five properties to each single control object is selected. The trials are filled-in simultaneously in order to avoid, when possible, common cases within them. Secondly, trials F to J are obtained, this time sort descending the  $M_*$  of the control sample. Trials A to E use a total of 139/231 (60%) perturbed galaxies with 13 common cases within them five. Likewise, trials F to J use 133/231 (58%) perturbed galaxies with 17 common cases within them all. Notice a trend of increasing common cases as the fraction of usage decreases<sup>8</sup>. In sum, the ten trials have a usage of 162/231 (70%, see Table A1).

<sup>6</sup> <https://bit.ly/2leelCX>

<sup>7</sup>  $M_*$  is preferred, for instance, over  $z$ , since it is easier to compare a quantity which has no need of more than two tenths to be significant ( $z$  is often expressed with more than two tenths).

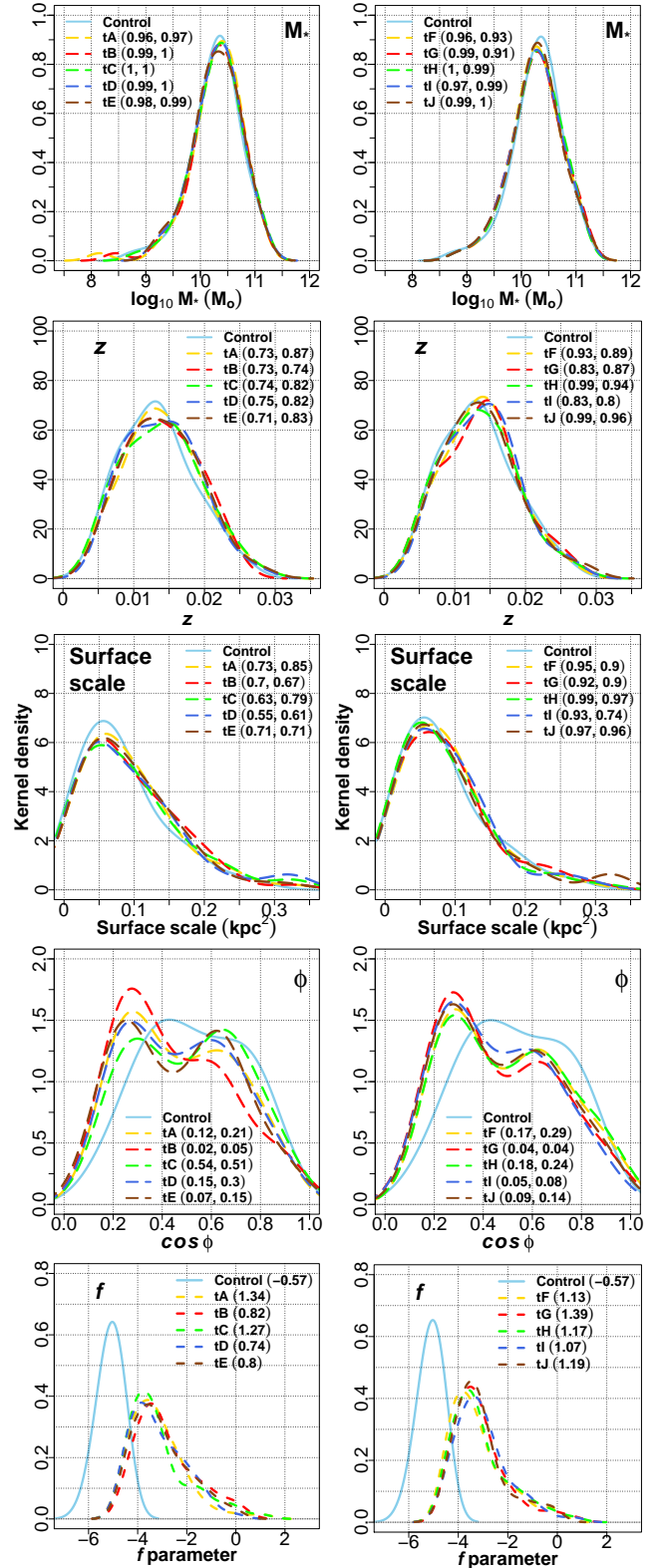
<sup>8</sup> A third set of five trials (not shown) with a usage of 150/231 (65%) has 9 common cases. However, beside the control sample, it has the less alike  $z$  distributions, the more unlike frequencies of objects according to the source of gas excitation, and so on.

Figure 1 (top) shows the contrasts in distributions for fundamental  $M_*$  and  $z$ . For the former, the ten perturbed samples tightly follow the distribution of the control one whilst results of the statistical tests are nearly one. For  $z$ , the dashed-line distributions closely follow the control one with statistical results of at least 0.7. The rest properties, surface scale,  $\cos \phi$  and  $f$  parameter are later treated in Section 3.4. Figure 2 illustrates the morphological group-galaxy colour relation. Notice that all panels show an increment of blue objects and a decrement of red ones as the morphological group becomes later. Frequencies of all perturbed samples by group and colour little differ from those of the control one. Figure 3 plots the CMD for each pair of comparisons. Similarly, frequencies and percentages of colour perturbed galaxies are well balanced with respect to those of control objects. Moreover, most of the area enclosed by the density contours overlap. At the statistical level, differences between each pair of probability distributions ( $D_{2DKS}$ , bottom-right) support the null hypothesis of a common parent distribution. Finally, the frequencies related to the dominant source of gas excitation are listed. The control sample consists of 52/10 SFG/AGN-like type objects. In the same way, contents of samples tA to tJ are 50/12, 51/11, 51/11, 52/10, 51/11, 49/13, 50/12, 50/12, 50/12, 49/13 SFG/AGN-like types respectively.

### 3.4 Sample comparison

Contrasts in spatial scales of the single star-forming regions and in galaxy inclinations with respect to the plane of the sky can be both sources of observational bias. Density estimations for the spatial or surface scale,  $\cos \phi$  and  $f$  parameter distributions are shown in Fig. 1 (see also Table A1). For surface scales, the dashed-line distributions resemble the control one with statistical results of at least 0.6. These scales directly depend on  $z$  so the density estimations and statistical results of the scales will always be as good as those of  $z$ . In contrast, the  $\cos \phi$  distributions are the odd case. The density estimations evidently differ: the perturbed samples are biased towards larger inclinations. We therefore relocate the coordinates of each spaxel by deprojecting them on those galaxies that show a disk component. The number of non-deprojected cases is larger for the perturbed samples (tA to tJ) consequence of their higher bias. Non-deprojected cases, *i.e.* low  $\cos \phi$  values for trials tA to tJ are 13, 17, 8, 11, 15, 12, 16, 13, 13, and 17 respectively. Likewise, they are 6 for the control sample. Regarding the  $f$  parameter distributions, skewness is used as a measure of normality. The control sample distribution, close to be fairly normal, is moderately (negatively) skewed. On the contrary, the distributions of the perturbed samples are positively skewed, most of them highly (outliers).

Having shown alike surface scales for resolved regions, we now explore contrasts in frequencies of star-forming regions among samples and per single galaxy. Table 2 lists these frequencies by splitting the control and perturbed samples according to the source of gas excitation. No known phenomenon prevents most of the available gas to turn into stars in SFG Blue and SFG LTS objects so both are the ones shown apart only for the sake of brevity. SFG Green and SFG Red types are included in the SFG subsample and are shown apart from Section 4 on. Even fairer comparisons will



**Figure 1.** Fundamental properties: Kernel density estimations for the distributions of fundamental  $M_*$  and  $z$  (top). Distributions of surface scale, inclination angle ( $\phi$ ) and  $f$  parameter are also included (middle to bottom). The perturbed samples, trials A to J, are shortened as tA to tJ. For  $M_*$  to  $\cos \phi$ , results from the Anderson-Darling (AD) and permutation (equal densities) tests are shown for each perturbed sample against the control one. The skewness ( $S$ ) as a normality test, is shown for the  $f$  parameter. Decisions are fairly normal ( $-0.5 \leq S \leq 0.5$ ), moderately skewed ( $-1 \leq S < -0.5$ ,  $0.5 < S \leq 1$ ) and highly skewed ( $S < -1$ ,  $S > 1$ ).

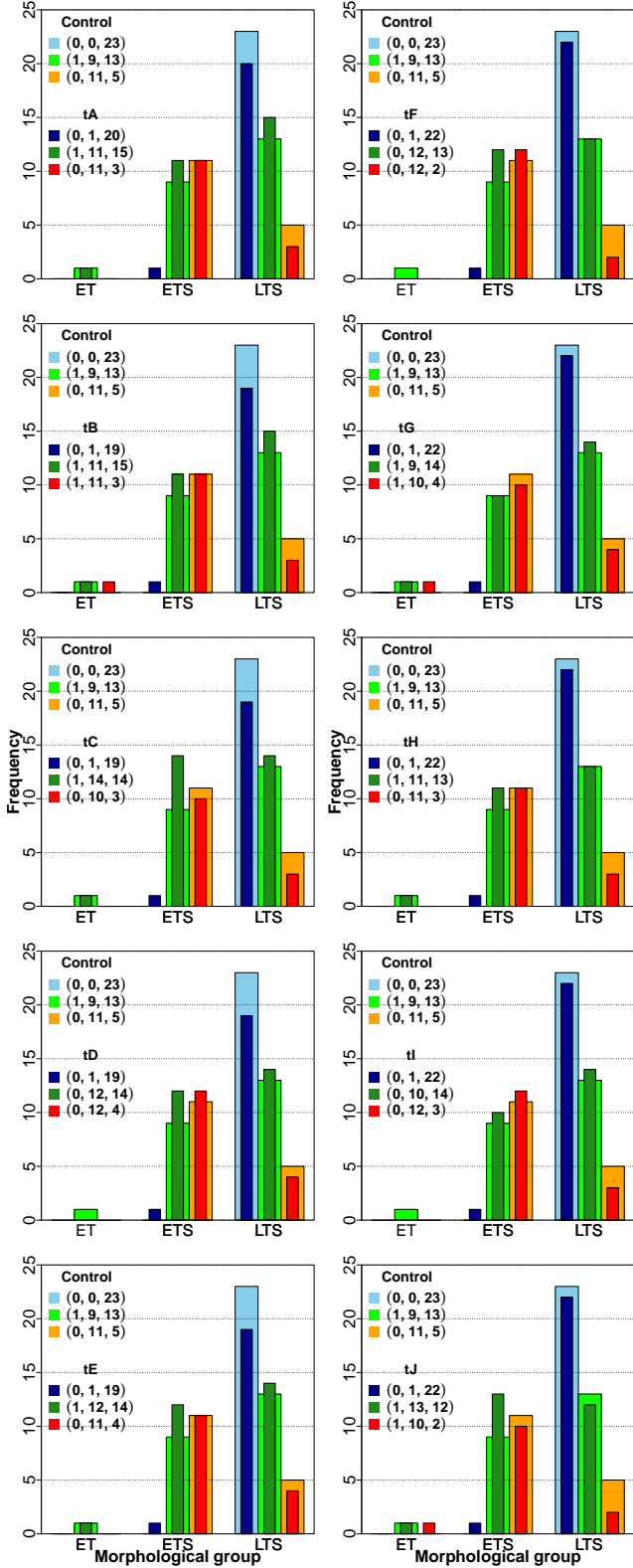


**Figure 2.** Fundamental properties: the morphological group-galaxy colour relation between control (Control) and perturbed samples (tA to tJ). Colour frequencies in parenthesis are ordered by morphological group (i.e. early type, ET; early type spiral, ETS; late type spiral, LTS).

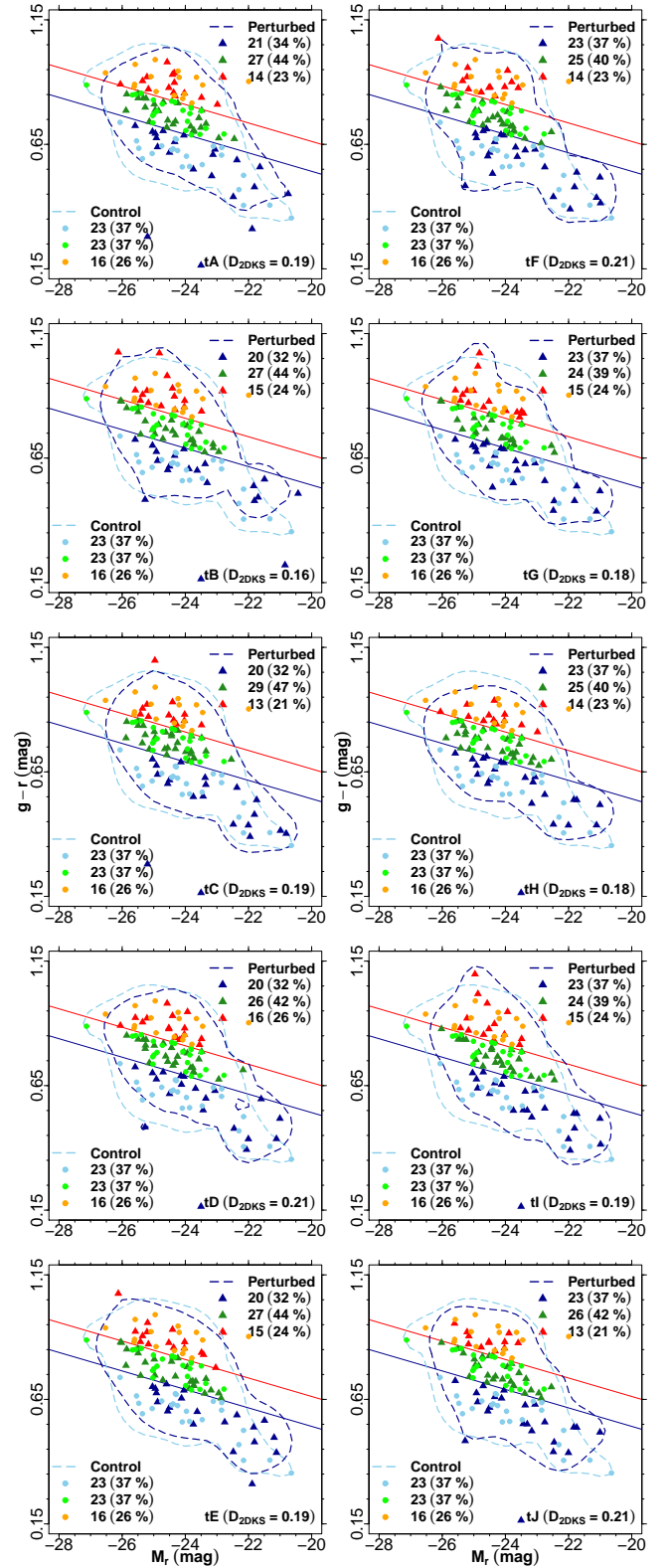


**Figure 3.** Fundamental properties: CMDs showing the distributions for control (Control) and perturbed samples (tA to tJ). The colour solid lines are explained in Section 2.2. The number of colour galaxies with their respective percentages, as well as 0.1 Kernel density contours (dashed lines) are indicated for each sample. From the 2D K-S/Peacock two-sample test, each bottom-right corner gives the maximum absolute difference ( $D_{2DKS}$ ) between each empirical cumulative probability distribution.

**Table 2.** Frequency summaries of galaxies (top) and star-forming regions (middle) as defined in Section 2.3.1. Star-forming region statistics per single galaxy (bottom).

	Control				Perturbed <sup>a</sup>			
	SFG Blue	SFG LTS	SFG	AGN -like	SFG Blue	SFG LTS	SFG	AGN -like
ETSs	...	...	12	9	1	...	13	11
LTSs	23	40	40	1	20	37	37	1
Total	23	40	52	10	21	37	50	12
ETSs	...	...	4396	1024	1462	...	5818	1900
LTSs	21 223	31 001	31 001	218	20 803	31 907	31 907	412
Total	21 223	31 001	35 397	1 242	22 265	31 907	37 725	2 312
median	925	746	628	98	894	713	628	127
mean	923	775	681	124	1060	862	754	193
$\sigma$	442	428	435	93	664	599	586	157

<sup>a</sup> Median values from gathering trials A to J (tA to tJ).

be conducted adopting this subsampling (not done in AGN-like galaxies due to the size limitation). Notice, from Table 2 (top), well balanced galaxy frequencies. In the case of the totals of star-forming regions (Table 2, middle), disproportions are the lack of SFG Blue early type spirals (ETSs) in control galaxies and the AGN-like case of perturbed galaxies almost doubling those frequencies of control ones (by a factor of  $\sim 1.9$ ). This last contrast is not expected since differences in galaxy frequencies are not as great as double. Even the respective  $z$  distributions exhibit no marked biases. Moreover, excluding the AGN-like subsample (with factors of  $\sim 1.3$  and  $\sim 1.6$ ), median and mean frequencies per single galaxy (Table 2, bottom) differ not much (largest factors are of  $\sim 1.1$ ). Anderson-Darling (AD) tests for the distributions of numbers of star-forming regions support this. Likelihoods are 0.59, 0.58, 0.75 and 0.48 for SFG Blue, SFG LTS, SFG and AGN-like respectively. In sum, numbers of star-forming regions in AGN-like galaxies are the most dissimilar ones.

### 3.5 H $\alpha$ flux percentage radii

All annular profiles compile single-galaxy data and depict each sample or subsample SP properties by concentric annuli. These are defined by the boundaries of deprojected radii which encircle percentages of the all-excitation H $\alpha$  flux (20, 40, 60, 80 and 100 %). From each galaxy set of spectra solved by STARLIGHT, the total H $\alpha$  flux is computed by ignoring the excitation source and flux outliers. The flux percentages are then computed and so the encircling radii. Since such those fluxes are meant for sectioning only, they are not extinction-corrected. Besides, their respective spectra sometimes show no H $\beta$  line emission detections (poor line S/N ratios). See Appendix B for an additional but important note on these annular profiles.

As noticed already, the H $\alpha$  flux, related to the data per se, is used to depict the radial extension instead of photometric extents such as the effective radius ( $R_e$ ). To prove the reliability of the encircling-H $\alpha$ -flux radii, Fig. 4 plots Kernel density estimations of the H $\alpha$  emission line distribution of our sampled galaxies as a function of  $R_e$  (half-light radius of the  $r$  band in an elliptical aperture, see W-14). Table 3 lists medians, 3rd quartiles (Qs) and standard deviations. Statistical test results between samples for the sets of these radial

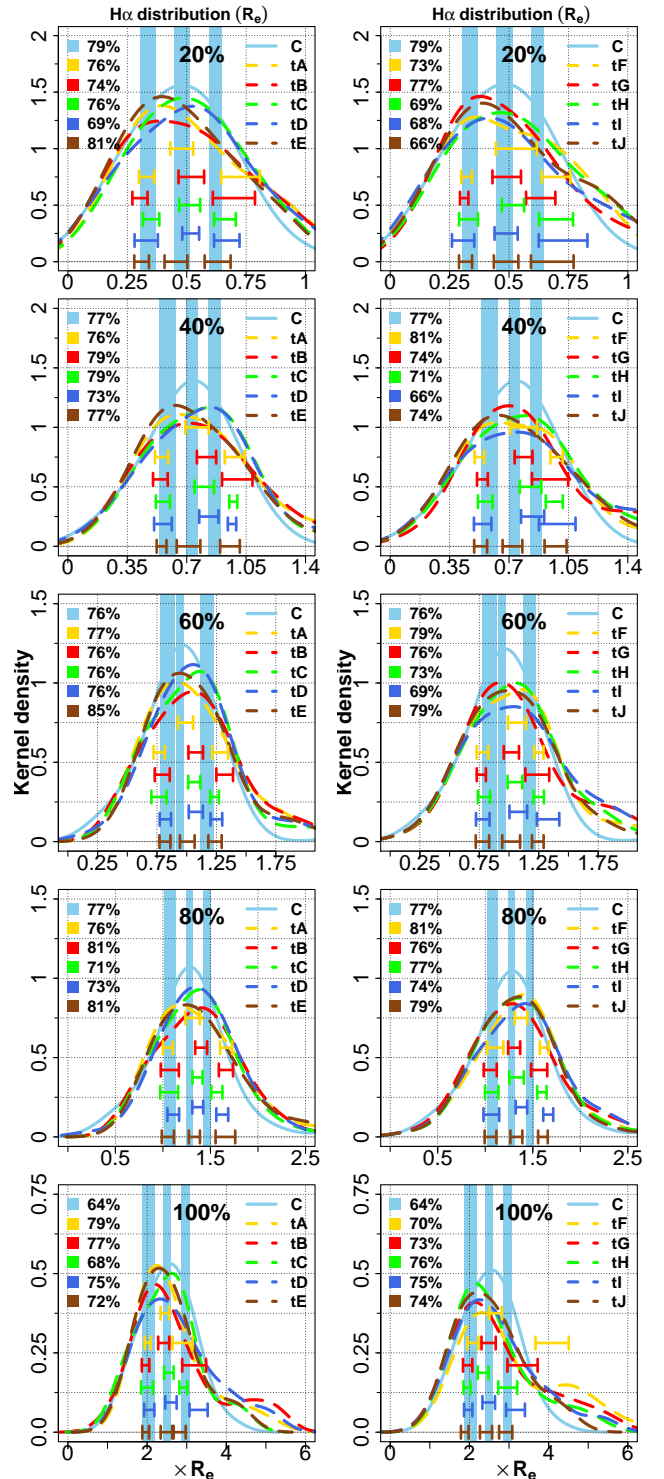


**Figure 4.** Kernel density estimations for our H $\alpha$ -flux-percentage radius/ $R_e$  fractions, *i.e.*, the H $\alpha$  emission line distribution as a function of  $R_e$  (20 to 100 %, from top bottom). Control (C) and perturbed samples, trials A to E and F to J (tA to tE, left and tF to tJ, right). At each left are the percentages of fractions (one fraction per galaxy) within  $\pm 1\sigma$  width centred at each distribution median. Light-blue columns are the Monte Carlo standard deviations (MCsds, *i.e.*  $\pm 1\sigma$  width from Monte Carlo simulations) corresponding to and centred at the 1st, 2nd (median) and 3rd quartiles (Qs) of the control distribution. Likewise, coloured ranges represent the same for each perturbed sample distribution.



fractions are also included. At each percentage radius/ $R_e$  fraction in Fig. 4 (panels 20 to 100%), numbers at left indicate the percentages of fractions (one fraction per galaxy) close to the median of each respective set, *i.e.*, within  $\pm 1\sigma$  width range centred in the median. In general, a bit more than a 70% of the fractions are near the median in each distribution. Moreover, medians of fractions in Table 3 are in good agreement with the standard definition of  $R_e$ . For instance, medians for the mid-radius (60%) are the ones closest to unity (see also Table A1). These  $H\alpha$  flux percentage radii are then credible distance normalizers and may be used as indicators of galaxy extensions.

From Monte Carlo simulations, standard deviations (MCsds) for medians, 1st and 3rd Qs are obtained for the distributions of percentage radius/ $R_e$  fractions. They are drawn as columns for the control sample, and as ranges for trials tA to tJ (see Fig. 4). If contrasting the ranges with respect to the columns, the former are biased towards higher fractions, specifically, medians and 3rd Qs. Also see that the curves are much different from the 1st Q on (right skewed). If comparing medians and 3rd Qs by computing fractions from Table 3, we find no significant difference for medians: 31/50 fractions advantage perturbed samples by  $<10\%$ . Third Qs are slightly different: 27/50 fractions advantage perturbed samples by  $>10\%$ . Differences in standard deviations are the most significant: 33/50 advantage perturbed galaxies by  $>20\%$ . We look at last at the statistical tests (AD-P) of Table 3. If arranging the likelihoods in the  $l > 0.5$ ,  $0.25 < l \leq 0.5$  and  $l \leq 0.25$  groups, frequencies for AD-permutation tests are respectively 6-4, 15-17 and 29-29. A likelihood for similitude of  $\leq 0.25$  describes the most both sample distribution functions. In sum, it may be said that the  $H\alpha$  line emission appears to be a little more dispersed for perturbed galaxies.

## 4 RESULTS

### 4.1 Resolved SFMSs

Galaxies with H II regions, small fractions of old stars and little light concentration yield the SFMS, the tight correlation of both global  $M_*$  and SFR. It has been confirmed that a local (resolved) correlation also holds for  $\Sigma_*$  and  $\Sigma_{\text{SFR}}$  (*e.g.* Sánchez *et al.* 2013; Cano-Díaz *et al.* 2016; González-Delgado *et al.* 2016; Hsieh *et al.* 2017; Cano-Díaz *et al.* 2019; Vulcani *et al.* 2019). Analyses which evidence the global correlation as a consequence of the resolved one have increased recently. However, Erroz-Ferrer *et al.* (2019) and Cano-Díaz *et al.* (2019) (hereafter CD-19) have shown that regions with low  $\Sigma_*$  noticeably flatten the resolved relation. CD-19 exhibit that below the  $7.5 M_\odot \text{ kpc}^{-2}$  threshold,  $H\alpha$  flux detection limits, apertures and other observational constraints affect the data and they warn about them in other surveys. Similarly, Hall *et al.* (2018) find that galaxies and regions of others spatially below this threshold do not follow the SFMS. Due to this issue, from this Section on and in Appendices B and C, we treat only star-forming regions above the CD-19 threshold.

Table C1 lists, in annular comparison sets, the linear regression coefficients of control and perturbed samples (tA to tJ) on the SFMS plane. Specifically, slopes for the same pre-

**Table 3.** Medians, 3rd quartiles (Qs) and standard deviations (median-3rdQ- $\sigma$ ) of the percentage radius/ $R_e$  fractions (*e.g.*  $\times R_e$ ). AD and permutation test results (AD-P) for each radial set of fractions between control and each perturbed sample (tA to tJ) are also listed.

H $\alpha$ flux percentage radii				
20%	40%	60%	80%	100%
Control				
0.48-0.62-0.27	0.73-0.86-0.30	0.94-1.17-0.33	1.28-1.47-0.40	2.50-2.96-0.63
tA				
0.48-0.73-0.33	0.76-0.98-0.38	0.99-1.28-0.40	1.31-1.67-0.48	2.45-2.89-0.89
0.27-0.26	0.22-0.18	0.20-0.24	0.16-0.12	0.41-0.18
tB				
0.52-0.70-0.34	0.82-1.00-0.44	1.08-1.32-0.49	1.40-1.66-0.60	2.42-3.19-1.09
0.24-0.23	0.11-0.11	0.06-0.10	0.06-0.09	0.21-0.06
tC				
0.51-0.66-0.29	0.80-0.97-0.36	1.06-1.23-0.38	1.36-1.57-0.43	2.55-2.91-0.77
0.54-0.80	0.21-0.36	0.17-0.28	0.23-0.37	0.81-0.76
tD				
0.52-0.67-0.27	0.83-0.97-0.33	1.08-1.25-0.35	1.37-1.62-0.38	2.60-3.30-0.98
0.46-0.49	0.24-0.28	0.24-0.44	0.26-0.34	0.18-0.16
tE				
0.45-0.63-0.31	0.71-0.95-0.38	1.00-1.24-0.42	1.33-1.66-0.56	2.49-2.82-0.75
0.81-0.61	0.36-0.28	0.19-0.51	0.12-0.23	0.75-0.39
tF				
0.53-0.70-0.31	0.79-0.98-0.42	1.07-1.25-0.47	1.38-1.62-0.62	2.66-4.09-1.31
0.28-0.25	0.17-0.21	0.12-0.19	0.09-0.30	0.02-0.01
tG				
0.49-0.63-0.29	0.79-0.94-0.37	1.02-1.24-0.45	1.30-1.57-0.52	2.49-3.34-1.14
0.51-0.36	0.21-0.16	0.22-0.24	0.44-0.38	0.10-0.01
tH				
0.52-0.70-0.28	0.83-0.97-0.34	1.05-1.25-0.37	1.33-1.60-0.46	2.35-2.97-0.96
0.32-0.30	0.22-0.21	0.20-0.24	0.34-0.39	0.27-0.04
tI				
0.49-0.73-0.34	0.84-0.98-0.41	1.08-1.33-0.46	1.38-1.66-0.51	2.49-3.16-1.00
0.23-0.11	0.08-0.02	0.05-0.03	0.08-0.13	0.29-0.15
tJ				
0.49-0.68-0.27	0.72-0.97-0.36	1.02-1.24-0.42	1.33-1.61-0.47	2.42-2.92-0.82
0.43-0.24	0.29-0.11	0.28-0.32	0.33-0.46	0.54-0.25

**Table 4.** Frequency summary from the annular comparisons between samples for all subsamples (see Table C1). Numbers in parenthesis are totals of star-forming regions and annular means. Columns titled as “Fig. 5” list the frequencies from the comparisons in Fig. 5. Acronyms (first column) mean frequencies of Different Slopes (DS), of Perturbed samples having the Flat-test slope (PF) and frequencies of Different Distribution functions (DD).

Annuli (H $\alpha$ flux percentages)					Fig.	Annuli (H $\alpha$ flux percentages)					Fig.	
20%	40%	60%	80%	100%	5	20%	40%	60%	80%	100%	5	
AGN-like (36 552, 7 310)						SFG Red (68 654, 13 731)						
DS	10/10	7/10	3/10	7/10	10/10	4/5	8/10	6/10	4/10	7/10	10/10	4/5
PF	0/10	0/7	3/3	1/7	10/10	1/4	3/8	4/6	0/4	0/7	3/10	1/4
DD	7/10	9/10	9/10	9/10	10/10	5/5	10/10	9/10	9/10	8/10	10/10	5/5
SFG ETS (122 322, 24 464)						SFG Green (208 180, 41 636)						
DS	8/10	10/10	9/10	8/10	10/10	5/5	8/10	6/10	3/10	4/10	8/10	4/5
PF	1/8	0/10	0/9	0/8	0/10	0/5	0/8	2/6	3/3	4/4	8/8	3/4
DD	10/10	10/10	9/10	10/10	10/10	5/5	10/10	9/10	9/10	10/10	8/10	5/5
SFG Blue (376 698, 75 340)						SFG LTS (531 210, 106 242)						
DS	9/10	10/10	10/10	2/10	3/10	3/5	10/10	10/10	10/10	6/10	5/10	5/5
PF	9/9	10/10	10/10	1/2	2/3	3/3	10/10	10/10	10/10	6/6	4/5	5/5
DD	9/10	10/10	10/10	9/10	9/10	5/5	10/10	10/10	10/10	6/10	10/10	5/5
SFG (653 532, 130 706)						All (690 084, 138 017)						
DS	9/10	10/10	10/10	5/10	5/10	5/5	9/10	10/10	10/10	7/10	8/10	5/5
PF	9/9	10/10	10/10	5/5	4/5	5/5	9/9	10/10	10/10	7/7	8/8	5/5
DD	10/10	10/10	10/10	8/10	10/10	5/5	10/10	10/10	10/10	9/10	10/10	5/5

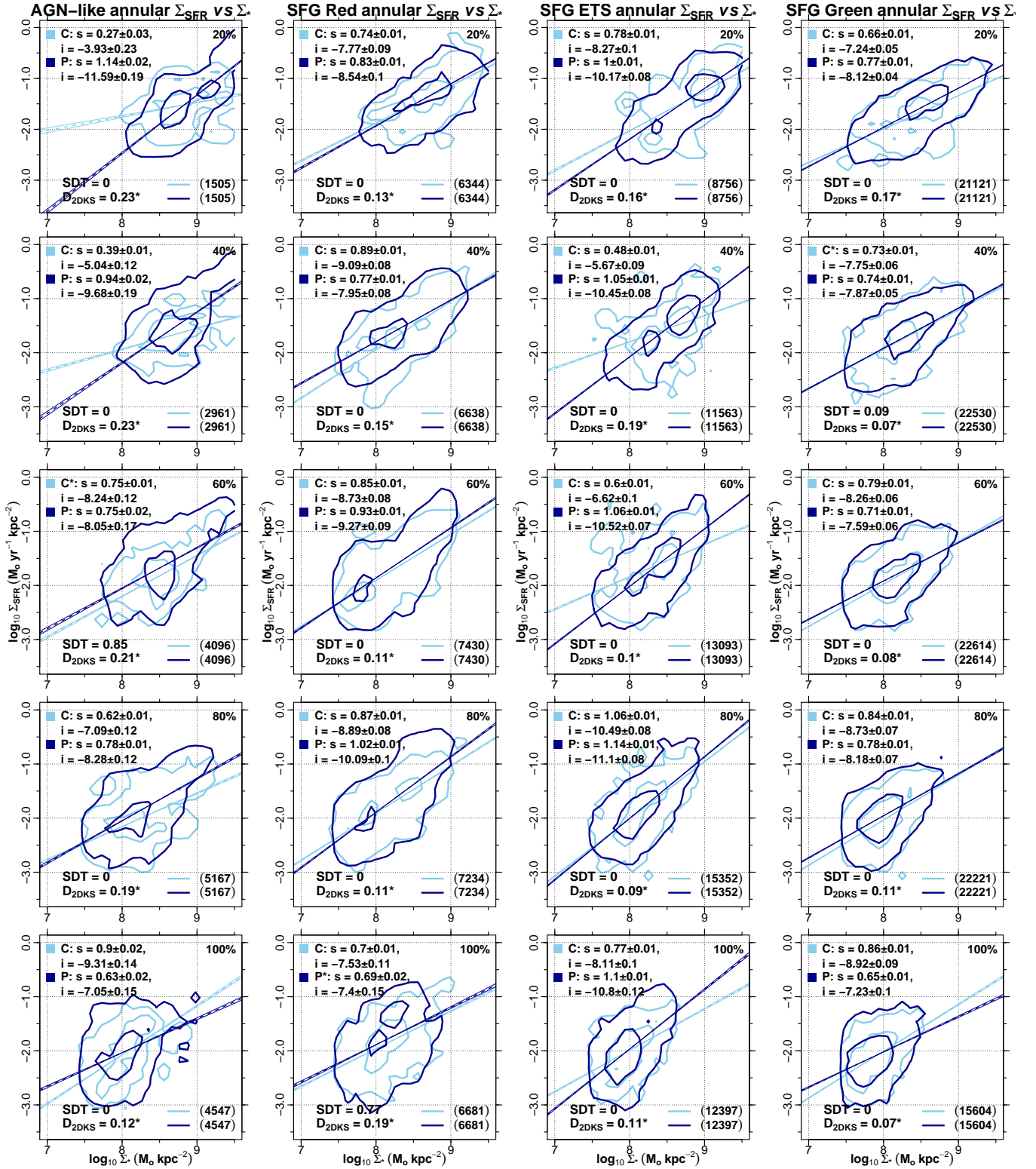


**Figure 5.** Annular-resolved SFMSs. The perturbed star-forming regions (dark blue) are paired with their control ones (light blue) closest in  $\Sigma_*$  (*i.e.*, paired by the minimum  $\Sigma_*$  difference). All star-forming regions in each comparison set (*i.e.* trials tA to tJ each one with its respective control sample regions, see Appendix C) are considered in order to get average linear model coefficients. From left to right: Kernel density estimations (0.1 and 0.9 contour densities from outside-in) of the star-forming regions inhabiting AGN-like, SFG Red, SFG ETS and SFG Green galaxies. Control (C) and perturbed (P) linear regression coefficients: slope ( $s$ ) and intercept ( $i$ ) (models for all annular sequences are statistically significant). Though not perceptible in all annuli, the error intervals are drawn for all fits. Asterisks indicate, from significance difference tests (SDTs), the sample (C or P) with  $s$  closer to that one if combining both-sample regions (Section 5.4). Likewise, SDTs are shown for each pair of sample slopes. 2D K-S/Peacock two-sample test differences ( $D_{2DKS}$ , Yuanhui 2017) are finally included. Asterisks indicate that both distribution functions come from a different parent distribution.

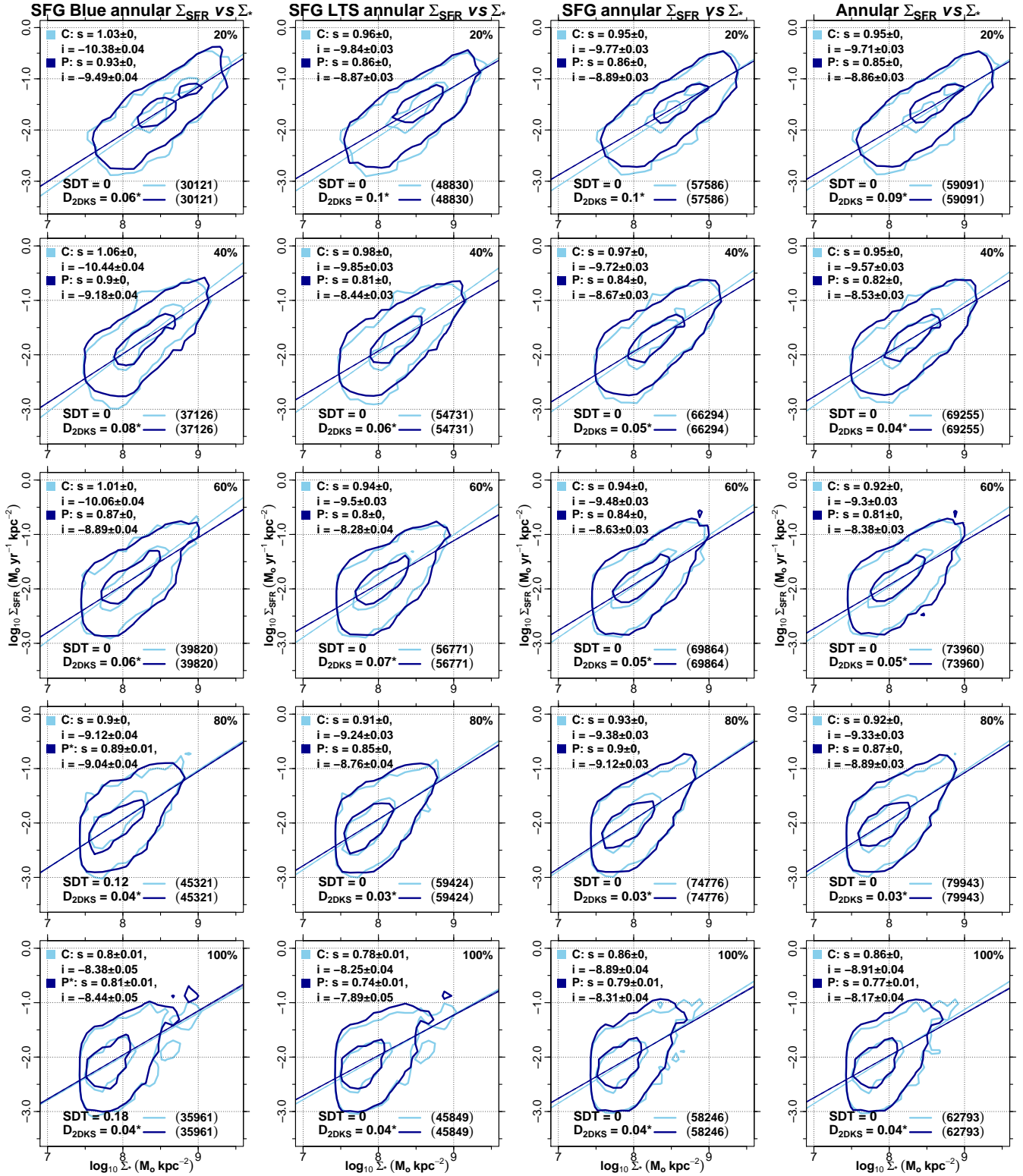


Figure 5. Annular-resolved SFMRs (cont.). Same caption as above but for SFG Blue, SFG LTS, SFG and all galaxies.

dicator ( $\Sigma_{*}$ ) across two models (control and perturbed galaxies) are compared<sup>9</sup>. To do so, an *interaction term* between

samples and  $\Sigma_{*}$  is included in the model function. In this way, the *p-value* of the interaction term represents a significance difference test (SDT) between both sample slopes. Importantly, sample slopes are suggested to be different when the SDT value falls below the statistical level. In each compar-

<sup>9</sup> All SP properties overall this work are compared at the closest (not equal)  $\Sigma_{*}$  of the star-forming regions (see Appendix B).

ison set of Table C1, slopes marked with \* are the closest ones to the slopes resulting from combining both sample data (a topic treated afterwards, Section 5.4). Only SDTs with values above the statistical level are considered for this and that slope with the highest test value is marked. On the other hand, for comparisons, only cases of different slopes are used. Lastly, from the K-S/Peacock two-sample test,  $D_{2DKS}$  differences marked with \* reject the null hypothesis of a parent distribution as the origin<sup>10</sup>. With all this in mind, we summarize Table C1 comparisons between samples for all subsamples in Table 4.

Starting with frequencies of Different Slopes (DS), annuli having those greater than 5/10 are identified. Notice that at least in 3/5 annuli this condition is satisfied. That is the case of SFG Green, SFG Blue and SFGs. SFG ETS and all galaxies meet the condition in all annuli. So, in general, models of linear regression (slopes) on the resolved SFMS differ between control and perturbed samples. Second, from the above cases of different slopes, we find those in which the Perturbed sample has the Flattest slope (PF). Similarly, we distinguish those annuli in which the fraction exceeds a half. This restriction is poorly met in AGN-like and SFG Red objects (2/5, 1/5 annuli respectively) and is not in SFG ETSs. For the others occurs the opposite: 3/5 annuli for SFG Green, 4/5 for SFG Blue and 5/5 for the rest. This means, for both samples, that the  $\Sigma_*$ - $\Sigma_{SFR}$  relation might be correlated with the galaxy subsample (the stellar mass concentration specifically). Finally for all annuli, and regardless of the subsample, the 2D distributions of control and perturbed samples point to differ in regard of their origins. All fractions of frequencies of Different Distribution functions (DD) are greater than a half.

To explore the mean trends of linear regression models of all samples on the SFMS plane, Fig. 5 plots all star-forming regions in the annular comparison sets of Table C1. In the same way, columns of Table 4 allusive to Fig. 5 list the annular frequencies result of the sample comparisons. DS frequencies are found in at least 3/5 annuli so, on average, linear regression slopes differ too. The previous trend of PF frequencies repeats: the lowest fractions belong to AGN-like, SFG Red and SFG ETS objects whereas a significant increment starts from the SFG Green subsample. As same as before, regardless of annulus and subsample, the 2D distributions do not share a parent one as a common origin.

Moreover, some important notes from inspecting Fig. 5.

- By concentric annuli:
  - (i) All positions of 0.1 and 0.9 contour densities clearly show a trend of both  $\Sigma_*$  and  $\Sigma_{SFR}$  decreasing from the centre (Maragkoudakis *et al.* 2017).
  - (ii) The standard deviations of both  $s$  and  $i$  diminish from the centre for control but remain rather constant for perturbed galaxies. Picturing the stellar dynamics might distinguish perturbed galaxies as having disordered SF processes along all annuli.
  - (iii) Excluding SFG Red objects, the highest  $D_{2DKS}$  dif-

ferences go inwards. This might support contrasts in the transfer of gas to the centres.

- By galaxy subsamples:

(i) Compared with those of all galaxies, the density distributions of AGN-like, SFG Red, SFG ETS and SFG Green objects are quite unlike. The most dissimilar distributions between samples belong also to these galaxies (greater  $D_{2DKS}$  differences). Section 5 explores whether these facts are consequence of the amounts of star-forming regions that inhabit each subsample (see Table 4).

(ii) As noticed already, a singular trend characterizes the flattening/steepening of the sample slopes. That trend might depend on the stellar mass concentration that according to the literature may distinguish our subsamples (AGN-like, SFG Red and SFG ETS objects distinguished by the highest  $\Sigma_*$  values, *e.g.* Appendix B). By finding steeper slopes for Sc-Scd/Sd-Sdm types in the disk-component SFMS, Catalán-Torrecilla *et al.* (2017) propose quenched SF in Sb-Sbc more massive disks. Following this, control AGN-like, SFG Red and SFG ETS galaxies would be at a quenching stage. The same for perturbed SFG Green, SFG Blue, SFG LTS, and SFG galaxies. Section 5 explores whether suppressions or (re)activations of SF (quenching or rejuvenation) are at play.

In sum, on the SFMS plane, star-forming regions in control and perturbed galaxies show models of linear regression that differ, inclinations of the model fits that depend on the galaxy subsample and 2D distributions with unlike origins.

## 4.2 Annular profiles

The distributions of the profiled SP properties along this work belong to all regions in the annular sets of comparisons of Table C1. So, as in Fig. 5, our profiles show the median trends across trials  $t_A$  to  $t_J$  all against the control sample. Figures 6 and 7 profile the SP age,  $\Delta\Sigma_{SFR}$ <sup>11</sup> and  $sSFR$ . “Differences” are the medians of the annular distributions of differences whilst symbols are both sample values giving those Differences. Line segments are the corresponding interquartile ranges (IQRs) of each respective distribution. Between samples, the distributions are compared by AD-permutation tests (likelihoods right below the profiles). Starting with age and excluding the AGN-like subsample, star-forming SPs are clearly older for perturbed samples. Differences and their IQRs are significantly extended above zero dex whereas most of the corresponding ones for AGN-like objects are well below. IQRs of symbols for AGN-like objects between samples clearly differ too. In perturbed galaxies of this type, SPs but the central ones tend to be younger.

Figure 7 (top) profiles the offsets with the annular SFMSs of the SPs in all galaxies regardless of the samples. Notice clear Differences, favorable for perturbed samples, in AGN-like, SFG Red and SFG Green objects. Major extensions of the IQRs are above zero in 3/5 annuli and IQRs of symbols in those annuli are the most dissimilar. Perturbed SFG LTS, SFG and all type galaxies show favorable slight Differences only in the centres. Major extensions of IQRs

<sup>10</sup> Due to our large annular-subsample sizes ( $n_1 n_2 / (n_1 + n_2)$ ), our  $Z_n$  values are near the asymptotic one of the Z statistic ( $Z_\infty$ , see Peacock 1983).

<sup>11</sup> Properly  $\Delta \log_{10} \Sigma_{SFR}$  ( $\log_{10} \Sigma_{SFR} - \log_{10} \Sigma_{SFR}^{\text{all sampled regions}}$ ).

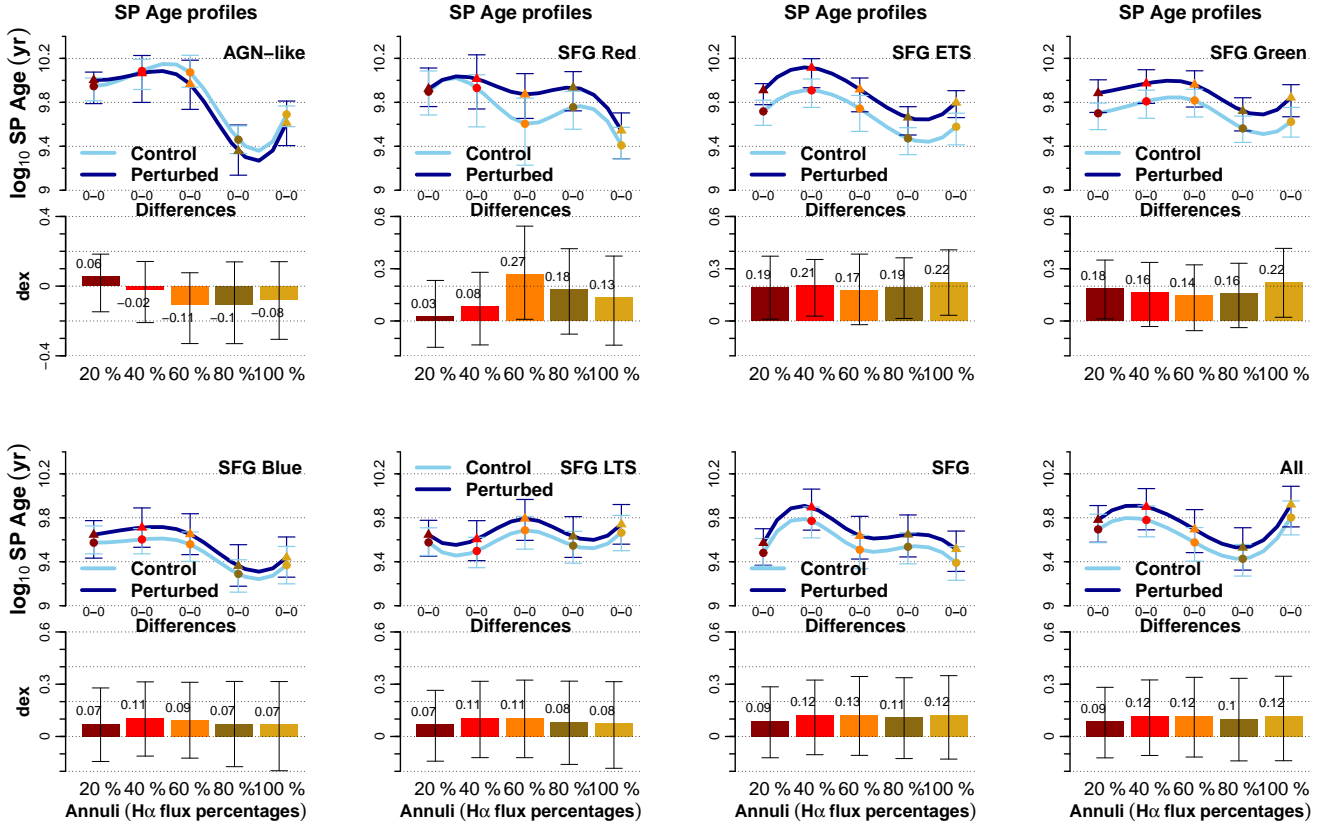


**Figure 6.** Annular profiles: SP age. All profiles use the amounts of annular star-forming regions per sample and subsample as in Fig. 5. Five consecutive-outward annuli denote the radial extension (see Section 3.5). “Differences” (bar heights by always subtracting the control values from the perturbed ones) are the medians of the annular distributions of differences (differences by pairing sample spaxels which are the closest in  $\Sigma_*$ ). Bar lines depict the interquartile ranges (IQRs, 1st to 3rd) of the distributions of differences. Symbols are both sample values giving each Difference. Symbol lines depict the IQRs of the annular distributions. On each pair of these, AD-permutation tests are performed (likelihoods right below the profiles).

of these Differences are clearly above zero. Total extensions of IQRs for central symbols of these perturbed subsamples are slightly biased towards higher offsets. For SFG ETS and SFG Blue subsamples, there are no consequential Differences (<10%). IQRs of their Differences are more balanced around zero. Moreover, only the control AGN-like subsample has negative offsets (reduced) along all annuli. Reduced cases are also those of SFG ETS, SFG Green and all types: no matter the samples, IQRs of central symbols are totally below zero and increments towards the periphery are apparent.

Notice the Differences and their IQRs of the sSFR (Fig. 7 bottom) in good agreement with those of the  $\Delta\Sigma_{\text{SFR}}$ . On this basis, all notes regarding the  $\Delta\Sigma_{\text{SFR}}$  are valid for the sSFR. Moreover, the threshold of Peng *et al.* (2010)<sup>12</sup> serves as a similar reference as the zero line for the  $\Delta\Sigma_{\text{SFR}}$ . Based on this, two similarities and two discrepancies can be seen between the  $\Delta\Sigma_{\text{SFR}}$  and sSFR profiles. These are respectively: 1) SFG ETS, SFG Green and all types keep showing clear increments from the centre (SFG LTS and SFG sSFR profiles now added); 2) unexpectedly, SFG Red objects centrally increased in  $\Delta\Sigma_{\text{SFR}}$  and above the threshold in sSFR; 3) centres of galaxies in all subsamples but SFG Red and

SFG Blue being below Peng *et al.* 2010 threshold (including their IQRs) and; 4) SFG Blue objects having a flat sSFR profile along the threshold. On the other hand, recall the younger SPs in perturbed AGN-like galaxies. Two facts now certainly explain this singularity: 1) regions in this subsample are increased in  $\Sigma_{\text{SFR}}$  and are currently more able to form stars (*e.g.* Sánchez *et al.* 2018b) and 2) perturbed AGN-like galaxies contain almost twice as many star-forming regions than their control analogues (Table 2).

The  $\Sigma_{\text{SFR}}$  is next profiled in Fig. 8. The agreement of the Differences and their IQRs between  $\Delta\Sigma_{\text{SFR}}$  and sSFR apparently persists in the  $\Sigma_{\text{SFR}}$ . This is a mere coincidence and has nothing to do with a common property ( $\Sigma_{\text{SFR}}$ ) influencing the computations.<sup>13</sup> The previous allows us to state, as in the case of  $\Delta\Sigma_{\text{SFR}}$  and sSFR, that the favorable Differences for perturbed samples are: 1) mostly dominant in AGN-like, SFG Red and SFG Green subsamples (3/5 annuli); 2) little, but evidently increased only centrally in SFG LTS, SFG and all subsamples and; 3) very likely, neither increased nor reduced in SFG ETS and SFG Blue ones. Notice, in addition, that the statistical tests on the annular distributions

<sup>12</sup> It suggests that, in the local Universe, a timescale larger than  $\log_{10} \text{sSFR} (\text{yr}^{-1}) = -10$  may announce the end of building the  $M_*$  budget of a galaxy to give place to quiescence.

<sup>13</sup> Footnote 9 and the three properties profiled differently (unlike shapes) argue against the fact of Differences belonging to only one particular region.

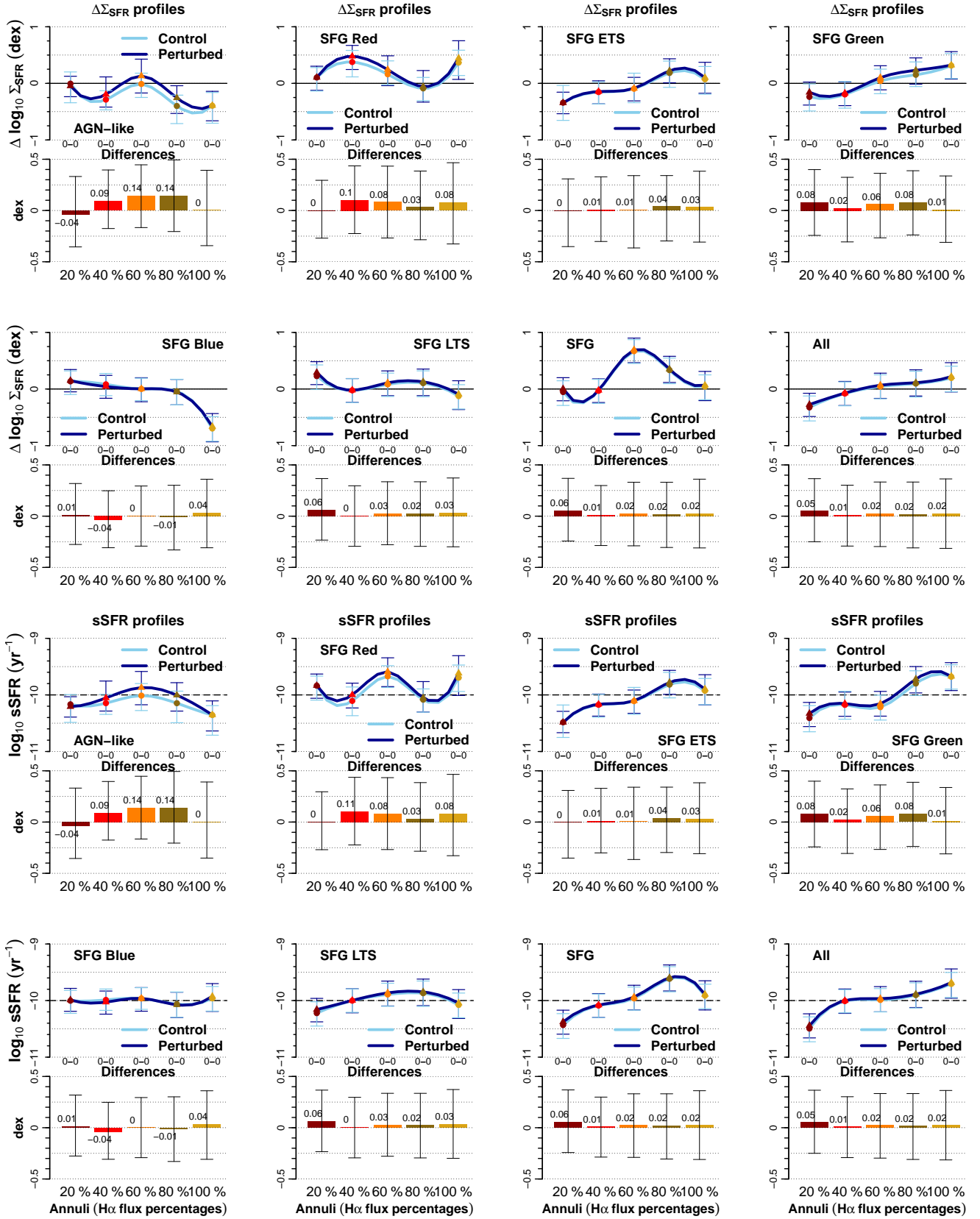


**Figure 7.** Annular profiles: (top)  $\Delta \Sigma_{\text{SFR}}$  using the annular linear fits of all sampled regions on the SFMS plane, (bottom)  $\text{sSFR}$  ( $\Sigma_{\text{SFR}} \Sigma_{\text{r}}^{-1}$ ) where dashed lines denote the Peng et al. (2010) threshold between SFGs and quiescent objects. Same information as in caption of Fig. 6.

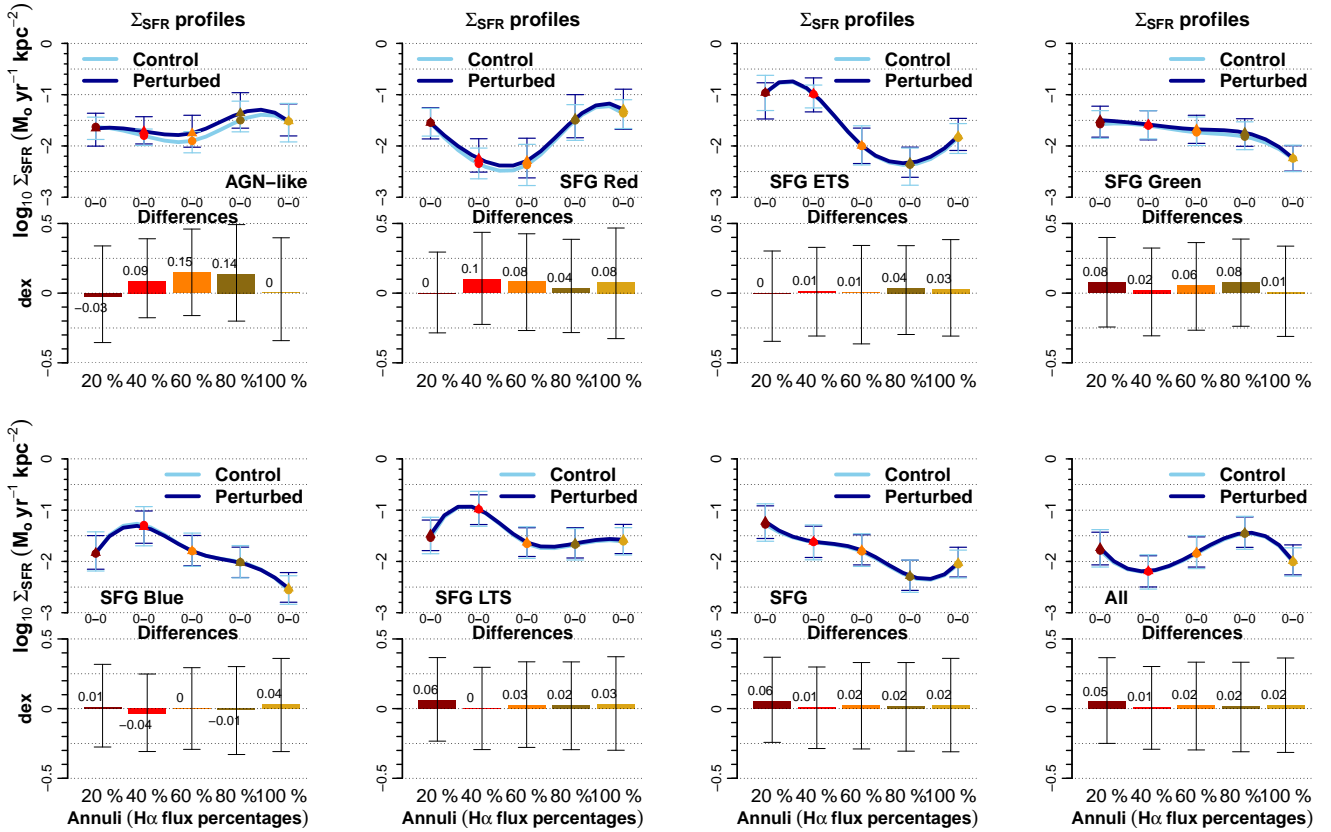


Figure 8. Annular profiles:  $\Sigma_{\text{SFR}}$ . Same information as in caption of Fig. 6.

result in the lowest likelihoods regardless of the property and subsample.

In general, the SFR properties of regions in perturbed galaxies are practically never inferior. This is despite the fact that these regions are older.

## 5 DISCUSSION

### 5.1 Amounts of regions and their SFMS distributions

In Section 4.1 we show that the density distributions on the SFMS plane of four subsamples: AGN-like, SFG Red, SFG ETS and SFG Green, are dissimilar compared with those of all subsamples. Between samples,  $D_{2\text{DKS}}$  differences are also greater among these subsamples than those among the other types. Table 4 lists the totals of star-forming regions used in each subsample. Notice a significant unbalance for AGN-like, SFG Red, SFG ETS and SFG Green subsamples with respect to the rest. To get a better understanding of a possible dependence of the SFMS distributions (the density distributions on the SFMS plane) on the amount of star-forming regions, in Fig. 9 we show the supplemental SFMSs. These help to characterize regions from all galaxies except those corresponding to each one of the four subsamples, *i.e.*, Fig. 5 1st part. Notice that the selection of these supplemental regions is done at the closest  $\Sigma_*$  values. These supplemental regions are distinguished either within control (gold contours) or within all the perturbed samples (red contours). The reasoning is the following: if the parameters derived

from these supplemental distributions are alike to those of Fig. 5 1st part, we would prove a dependence on the amount of regions. The contrary would mean that the SF processes (which characterize the regions and the supplemental ones) are different.

It turns out from Fig. 9, that SDTs point to equal slopes in only four annuli: two for SFG Red (20 and 80 % annuli, red and gold squares) and one for SFG ETS and SFG Green each (100 and 100 % annuli, gold and red squares, respectively). Regarding  $D_{2\text{DKS}}$  differences, all suggest that the density functions being compared do not have their respective origins in a common parent distribution. In sum, there are no similitudes between regions and their supplemental ones, at the closest  $\Sigma_*$  values and at the same number of regions for the perturbed samples and the control one. The dissimilarities between density distributions mentioned above do not depend neither on the amounts nor on the stellar mass concentration of the regions. On the other hand, by looking at the parameters comparing both supplemental regions between samples (bottom-right in all panels of Fig. 9), in 18/20 annuli, the SDTs suggest different slopes. From these frequencies, the fit corresponding to perturbed samples (red) is the flattest in 16 cases ( $D_{2\text{DKS}}$  differences also point to uncommon origins). Therefore the linear fits, either flatter or steeper, do not depend on the  $\Sigma_*$  of the regions but on some other property characterizing the galaxy types defining our subsamples. A possible explanation involving the  $M_*$  along with the perturbation parameter is treated in Section 5.3.

The one certainty is that most of the slopes for perturbed objects are flatter, than the corresponding ones for

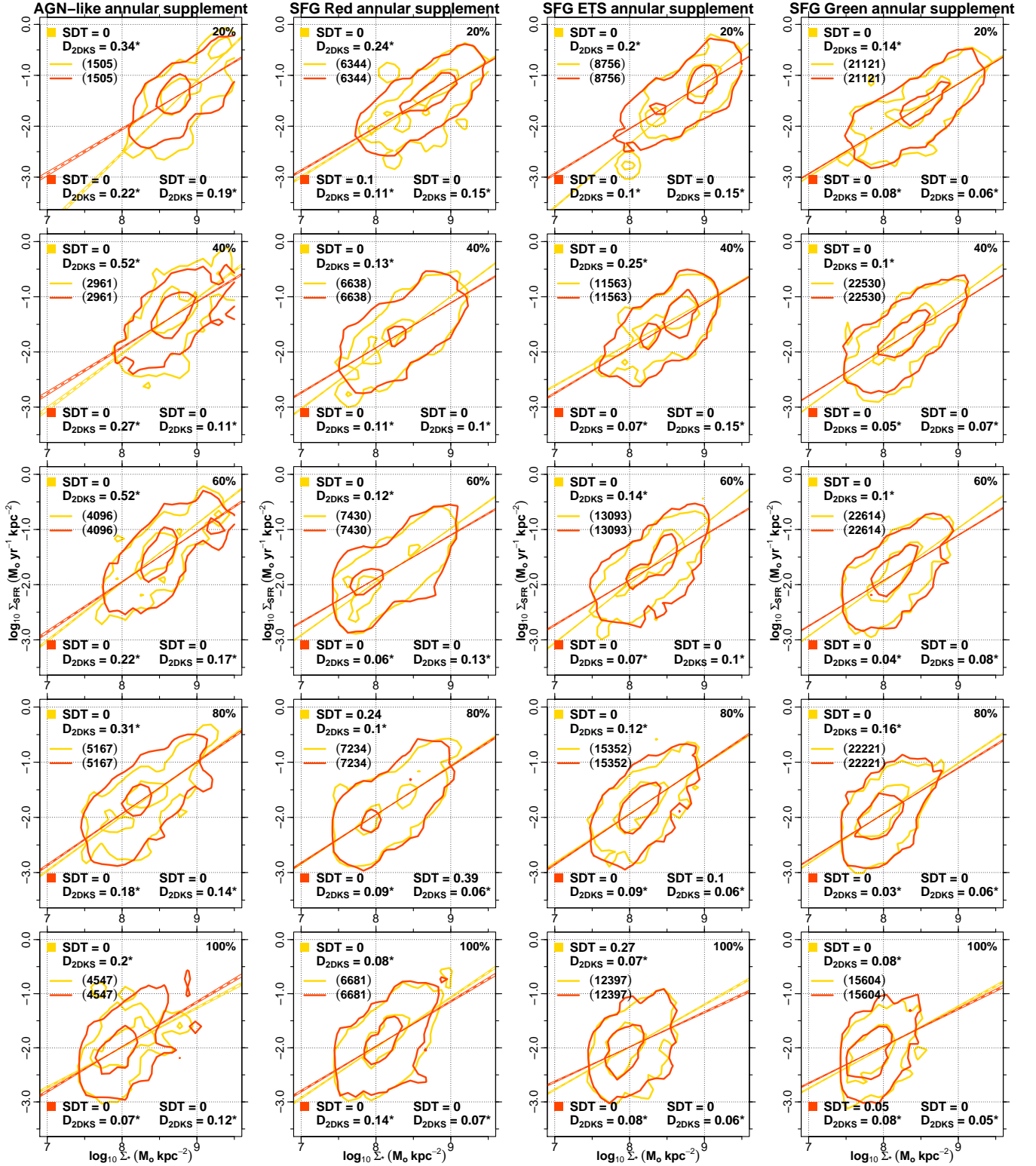


**Figure 9.** Supplemental, annular-resolved SFMSs. Perturbed star-forming regions (red) are paired with their control ones (gold) at the closest  $\Sigma_*$ . All supplemental star-forming regions in each comparison set (*i.e.* trials tA to tJ each one with its respective control sample regions, see Appendix C) are considered. From left to right: Kernel density estimations (0.1 and 0.9 contour densities from outside-in) of the supplemental star-forming regions corresponding to AGN-like, SFG Red, SFG ETS and SFG Green galaxies. Models for all annular sequences are statistically significant (error intervals are drawn for all fits). SDTs and  $D_{2DKS}$  differences (asterisks indicate both distribution functions coming from a different parent one) following colour squares (gold, control; red, perturbed) give the test results between regions (Fig. 5 1st part) and their supplemental ones within the same sample. SDTs and  $D_{2DKS}$  differences at the bottom-right give the results between supplemental regions only.



control objects, at the  $\Sigma_*$  values closest to those ones found in AGN-like, SFG Red, SFG ETS and SFG Green types. Concluding, the dominant trend for the galaxies in this study (*i.e.* the majority of regions, see Table 4) is that perturbed ones show lowered intensities of the SFR with increasing stellar mass density.

## 5.2Suppressions and/or (re)activations of SF

Section 4.1 shows slopes with a peculiar behaviour on the SFMS plane. These are flatter and steeper, for control and perturbed galaxies respectively, in AGN-like, SFG Red and SFG ETS objects. Then the slopes switch, to either flatter or steeper, in SFG Green, SFG Blue, SFG LTS, SFG and all objects. Since the former group of subsamples is distinguished by higher concentration of stellar mass (see Appendix B), this peculiar slope behaviour might depend on  $\Sigma_*$ . In the scenario proposed by Catalán-Torrecilla *et al.* (2017), control AGN-like, SFG Red and SFG ETS galaxies would be at a quenching stage (same for those in perturbed SFG Green, SFG Blue, SFG LTS and SFG subsamples).

However, the results in Section 5.1 suggest that this may not be the case. Steeper slopes for regions in perturbed galaxies do not repeat at stellar mass densities which are the closest to those found in AGN-like, SFG Red, SFG ETS and even SFG Green objects. To clarify on this matter, the SFR ( $\Delta\Sigma_{\text{SFR}}$ ,  $s\text{SFR}$  and  $\Sigma_{\text{SFR}}$ ) profiles (Figs. 7 and 8) are reviewed for traces of suppression (quenching) and/or (re)activation (rejuvenation) of SF. Along each property scale, we contrast the positions of central values relative to those ones of the rest annuli. This approach is justified since changes in central regions (either enhancement or suppression) dominate the regulation of SF (Ellison *et al.* 2018a).

Starting with the  $\Delta\Sigma_{\text{SFR}}$ , SFG Blue and SFG LTS galaxies show central offsets above the rest annuli. In AGN-like objects, the central offset exceeds three of the rest annuli. SFG Red galaxies have its central offset below three of the rest annuli. The rest galaxy types show evident increments from the centre. Regarding  $s\text{SFR}$ s, the SFG Red subsample central annulus appears diminished by two annuli. Though quite aligned with all the rest, the central annulus in SFG Blue objects is diminished by two annuli. The central  $s\text{SFR}$ s and their IQRs in the rest subsamples evidence increments as going outwards (not at all in AGN-like objects due to the periphery). Lastly, the central  $\Sigma_{\text{SFR}}$  is diminished against the periphery in AGN-like and SFG Red subsamples. The same may be for all subsamples together. In SFG Blue and SFG LTS types, the central intensity is just diminished against that one of the next annulus. It is in SFG ETS, SFG Green and SFG objects where the centre is evidently dominant. Summarizing, the three profiles show diminished central values (against one annuli at least) in AGN-like, SFG Red and all subsamples. These three types of galaxies are then the clearest ones suffering from quenching.

Though AGN-like types are clear candidates for quenching, some attributes distinguish the perturbed objects. Their age profile indicates younger SPs along all annuli but the central one. In the middle (40, 60 and 80% annuli), perturbed samples clearly advantage the control one in the three SFR profiles just discussed. In average, numbers of star-forming regions for perturbed samples double control fre-

quencies. This all suggests rejuvenation of the mid-annular SPs in perturbed AGN-like objects.

Finally, the favorable central Differences (Figs. 7 and 8) for perturbed SFG LTS, SFG and, specially, all galaxies, place control objects as the closest candidates for quenching. An interesting fact is why perturbed galaxies mostly exhibit flatter slopes on the SFMS plane (Table 4 and Section 5.1). Perhaps the influence of stellar mass density is somehow weakened. Something else might be regulating the SF in perturbed galaxies.

## 5.3 A correlation between SF and tidal effects

Peng *et al.* (2010) estimate the mean local density of galaxies at different redshifts. There are no detectable differences in SFMS and mean  $s\text{SFR}$  for SFGs between the lowest and highest density Qs. Ellison *et al.* (2018a) find a similar result. By doing a dynamical analysis, Erfanianfar *et al.* (2016) compile secure X-ray-detected galaxies to explore the SFMS too. At  $0.15 < z < 0.50$  they find a flattening caused by red-disk dominated galaxies. Notice that the galactic vicinities in these analyses are expressed by density fields whereas our approach sets the need of ensuring physically related objects, *i.e.* tidally-related, particularly. As a result, on the SFMS plane, most of the star-forming regions in perturbed galaxies reproduce flatter linear models than those ones for regions in control objects (Section 4.1). This  $\Sigma_{\text{SFR}}$  reduction with  $\Sigma_*$  points to quenched SF since, indeed, SPs in the perturbed objects are mostly older. However, this assumption is questionable since regions in perturbed objects are practically never inferior in the SFR profiled properties (Section 4.2). Contrasts are clearly favorable for perturbed AGN-like, SFG Red and SFG Green galaxies. For perturbed SFG LTS, SFG and all galaxies, contrasts are also favorable, though only in the centres. Though the SFR profiled properties confirm that a SF suppression has likely started in the centres (Section 5.2), this is regardless of either control or perturbed samples. Moreover, SPs in perturbed AGN-like objects are younger than SPs in their control analogues and the SFR profiled properties of the former are evidently higher. In sum, the flattening on the SFMS plane may not be due to SF quenching but due to a less dependent  $\Sigma_{\text{SFR}}$  on  $\Sigma_*$ . Tidal effects might be contributing to drive SF in these regions. This hypothesis would explain the (sometimes little but perceptible) contrasts in the SFR properties.

A possible correlation with tidal effects is then explored. We first combined our resolved results alongside the  $f$  parameter global measurements (defined in Section 3.1). When pairing the spaxels at a specific value of  $\Sigma_*$  (the annular median of a galaxy in any sample or the median difference between both annular sets of a galaxy in a sample and the rest galaxies in the other sample) there are always cases of galaxies in a sample with more than one  $\Sigma_*$  value as the closest to another one of another galaxy in the other sample. This issue makes  $f$  parameters to have more than one resolved property value at the same time, having, as a consequence, perceptible effects on the correlation. Notice, in contrast, that our resolved-to-resolved correlations are free from this issue. Figure 10 uses therefore integrated SFR properties of the samples at tight  $M_*$  distributions (see Fig. 1). As we previously did (Figs. 5 and 9), the average trend is shown for perturbed samples by plotting them altogether

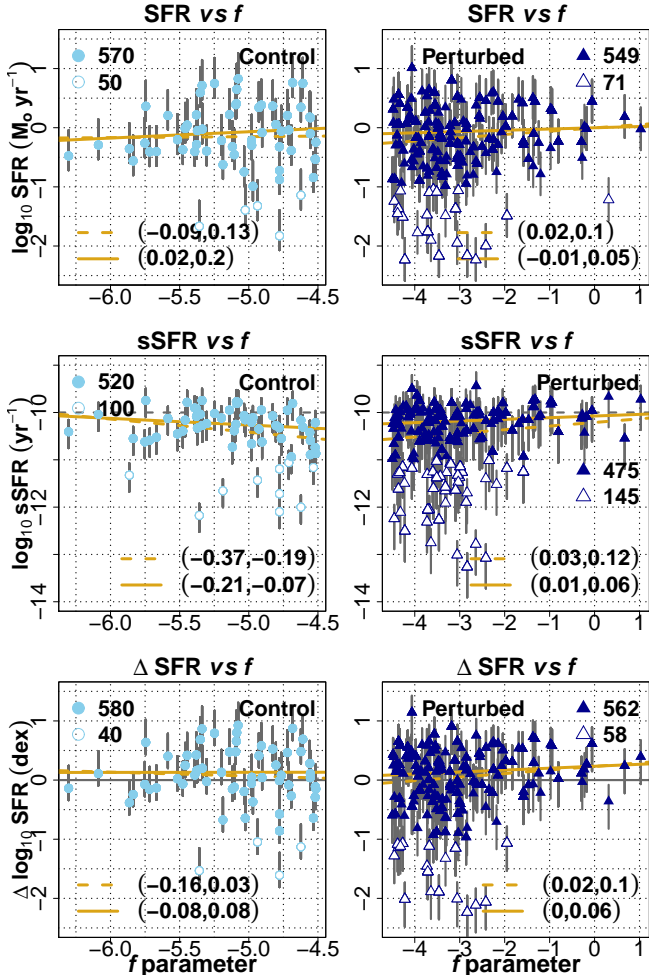


**Figure 10.** The SFR properties against the  $f$  parameter for control (Control) and perturbed (Perturbed, tA to tJ) samples. Black-dashed lines for the sSFR as the Peng *et al.* (2010) threshold between SFGs and quiescent objects. The SFR offset ( $\Delta$ SFR) is computed from a linear fit (SFMS) on the data of all samples. Line segments of points as the IQRs of each property distribution in each sample. Numbers after filled and empty symbols are the frequencies of points above and below, respectively, the thresholds of  $-1$ , for SFR and  $\Delta$ SFR, and  $-11$ , for sSFR. Gold lines are robust linear model fits, for all points (dashed), and for filled ones (solid). Intervals at 95 % confidence level (bottom) enclose the true values of the model slopes (gold fits). Complementary statistical results in Table 5.

alongside versions of the control set. From robust model regression, 95 % confidence intervals of the resultant slopes (gold lines) are included. Moreover, Table 5 lists the summary of the linear model and correlation results. By looking at the gold dashed lines in Fig. 10, notice positive intervals for perturbed samples and negative lower ends for the control one. From the corresponding slopes, “dashed” rows in Table 5, perturbed samples have both linear model and correlation  $p$ -values below the statistical level. There seems to be a little but detectable increment of the SFR properties in perturbed galaxies with  $f$ . By definition, galaxies in the control sample are not experiencing gravitational torques that disturb their secular growth of stellar mass. Intervals and linear fits should be roughly balanced and flat, meaning that the tidal perturbation scale for the control sample is rather

**Table 5.** Summary of results for the SFR properties against the  $f$  parameter. Robust linear model slope  $s$ , its standard error  $e$  and model  $p$ -value. Pearson correlation coefficient ( $r_p$ ) and related  $p$ -value. “dashed” and “solid” rows in reference to the linear fits of Fig. 10 (dashed and solid gold lines).

	Control					Perturbed				
	$s$	$e$	$p$ -value	$r_p$	$p$ -value	$s$	$e$	$p$ -value	$r_p$	$p$ -value
	$\log_{10}$ SFR ( $M_{\odot} \text{ yr}^{-1}$ )									
dashed	0.017	0.056	0.760	-0.007	0.867	0.055	0.021	0.006	0.114	0.004
solid	0.107	0.047	0.021	0.082	0.050	0.021	0.017	0.210	0.061	0.155
	$\log_{10}$ sSFR ( $\text{yr}^{-1}$ )									
dashed	-0.276	0.046	0	-0.213	0	0.077	0.022	0.001	0.136	0.001
solid	-0.140	0.034	0	-0.201	0	0.035	0.012	0.005	0.134	0.004
	$\Delta \log_{10}$ SFR (dex)									
dashed	-0.066	0.050	0.180	-0.086	0.033	0.060	0.019	0.002	0.129	0.001
solid	0.002	0.042	0.964	-0.025	0.550	0.033	0.016	0.035	0.090	0.033

unimportant. If we now look on how the perturbed galaxies are distributed, we notice scarcities of high values for high parameters along with abundances of low values for low parameters.<sup>14</sup> To measure the effect of these unbalances, we recalculate the slope confidence interval and correlation coefficient for points  $\geq \log_{10} -1 M_{\odot} \text{ yr}^{-1}$ ,  $\geq \log_{10} -11 \text{ yr}^{-1}$  and  $\geq -1$  dex, for the SFR, sSFR and  $\Delta$ SFR respectively (gold solid lines in Fig. 10 and “solid” rows in Table 5). We find, for the perturbed samples, that though the intervals are reduced, slopes keep on being most likely positive and that the slope and correlation coefficient fail now on being significant only for the SFR. For the control sample, the only property that strongly varies is precisely the SFR. Since sSFR and  $\Delta$ SFR increments continue for perturbed galaxies, we may conclude that tidal perturbations play somehow a role as a SF driver.

In contrast, Catalán-Torrecilla *et al.* (2017) find  $M_{*}$  as the absolute driver. In this regard, we recall the trend of steeper slopes (on the SFMS plane) for regions in perturbed AGN-like, SFG Red and SFG ETS subsamples. The reason may certainly involve the characteristic  $M_{*}$  values for galaxies of these types. Perhaps  $M_{*}$  is too dominant so any effect of tidal perturbations (flattening included) is wiped out. We explore the  $M_{*}$ - $f$  parameter distributions for only perturbed galaxies. The ones in these three types are biased towards higher stellar masses and towards lower perturbation parameters. The opposite occurs for galaxies in the rest subsamples. Unfortunately, the anticorrelations result of comparing both global measurements are not statistically significant.

#### 5.4 An effect of perturbed galaxies on the SFMS

Cano-Díaz *et al.* (2016) report a SFMS of  $s = 0.72$ ,  $i = -7.95$  with  $\sigma = 0.16$  dex. As same as CD-19, who obtain  $s = 0.94$ ,  $i = -10.00$  and  $\sigma = 0.27$  dex, we use the OLS method and their threshold in  $\Sigma_{*}$ . We neither intend to compare the global and local SFMSs within our data, nor to explore the flattening below the threshold. Therefore, we do not bin the data as CD-19 do. All star-forming regions in all samples give  $s = 0.84$ ,  $i = -8.69$  with  $\sigma = 0.34$  dex. Regions in the control sample give  $s = 0.87$ ,  $i = -8.94$  with  $\sigma = 0.33$  dex whereas

<sup>14</sup> These profusions mostly consist of AGN-like and early type objects the ones characterized by the oldest SP median ages.

**Table 6.** Samples hosting the best representative linear regression models (slopes) of those ones when compiling the data of both samples in each respective annular comparison set (see Table C1). Perturbed samples are labeled as usually (tA to tJ). The control one (C) has an additional letter which indicates to what perturbed sample is compared to. Small fonts indicate that the slopes are the flattest ones of each set. “f1” gives the frequencies of best representatives. “f2” gives the frequencies where the sample slope is the flattest one (small fonts) and “f3” tells, from f2, the cases that belong to the perturbed sample.

	Annuli (H $\alpha$ flux percentages)												f1	f2	f3			
	20%			40%			60%			80%			100%					
AGN-like	tD			tB tD tI tJ			tA tB tC tD tE tF tG tH tI tJ			tA tB tC tD tE tF tG tH tI tJ			tA tB tD tE tH tI			28/50	13/28	12/13
SFG Red	tA tB tC tD tE tG tH	CA CB CC CD CE		tB tC tD tE tG tH tI tJ				tG tH tI				tG tJ			25/50	8/25	7/8	
SFG ETS	CB CE CG CI	...		CG				CA CB CC CD CE CF tG tH tI tJ				...			15/50	12/15	0/12	
SFG Green	tD CG	tB CC tD CE CH CJ		tA tB tE tF tH tI tJ				tB tE tF tH tJ				27/50			18/27	15/18		
SFG Blue	CA CC tG	...		CC				tA tB tC tD tE tF tG tH tI tJ			tA tB tD tE tG tH tI tJ	22/50			11/22	10/11		
SFG LTS	CA CE	...		...				tA tC tE tF				tA tB tD tE tJ			11/50	5/11	5/5	
SFG	CA CE	CA		tA tE				tA tB tC tE tF tH tI tJ				tA tB tD tE tJ			18/50	13/18	13/13	
all	CA CE	CA		tE				tA tC tE tF tI				tA tB tC tD tE tJ			15/50	11/15	11/11	
f1	23/80			17/80			30/80			54/80			37/80					
f2	9/23			3/17			16/30			37/54			26/37					
f3	4/9			2/3			14/16			27/37			26/26					

regions in all perturbed samples give  $s = 0.81$ ,  $i = -8.44$  with  $\sigma = 0.35$  dex. The following remarks emerge from this. First, the sequences reported above still come from pairing the star-forming regions at the closest  $\Sigma_*$  (see Fig. 5 for all galaxies). Second, our scatters are as high as the ones reported by Maragkoudakis *et al.* (2017), Hall *et al.* (2018) and Vulcani *et al.* (2019). And last, we look for any effect perturbed galaxies may cause on the SFMS.

The high scatters are due to systematic diversities and subgalactic population generalities in the sequences of the galaxies analysed by Maragkoudakis *et al.* (2017), Hall *et al.* (2018) and Vulcani *et al.* (2019). Hall *et al.* (2018) add the varying global environments where galaxies above the CD-19 threshold belong to. In our case, the fact of SF properties not only driven by stellar mass (Section 5.3) may be considered a cause too.

Concerning the last remark, Table C1 lists the linear regression results in annular comparison sets. Slopes marked with \* are the best representatives (closest ones from SDTs) of the slopes resulting from compiling both sample data in the corresponding comparison set. Table 6 lists the samples, either perturbed (tA to tJ) or control (initial C), hosting these representatives. Small fonts indicate that the slope is the flattest of the set (see Table C1). “f1” gives the frequencies of best representatives found. “f2” follows suit for the flattest slopes in each set. Lastly, “f3” tells the frequencies where the flattest slope belongs to the perturbed sample. Notice first from Table 6 that the frequencies of best representatives, f1, can not be ignored either annularly (row) or by subsample (column). They represent, at least, 21% (17/80, 40% annulus) and 22% (11/50, SFG LTS subsample) respectively. Similarly, from these representatives, the frequencies of being the flattest slope, f2, are far from being unimportant either annularly or by subsample too. They represent 18% (3/17, 40% annulus) and 32% (8/25, SFG Red subsample) respectively and even more. Finally, from these f2 frequencies, the cases in which the perturbed sample is majority, f3, are all but the 20% annulus (4/9), and the SFG ETS (0/12) subsample. We conclude from this all that perturbed galaxies tend to flatten the SFMS.

Few best representatives emerge from Fig. 5 (5/40). The reason is that the probability of finding the best match gets

reduced with the accuracy of the model, *e.g.* very low slope errors sometimes of the order of zero (thousandths). Though the frequencies of these representatives are favorable for perturbed galaxies (3/5), the few cases prevent us from doing a meaningful analysis.

## 5.5 Central and off-central distinctions

Barrera-Ballesteros *et al.* (2015) compare the EW (H $\alpha$ ) distributions of CALIFA survey merging and isolated SFGs. Their results are based on a central and an extended projected apertures. Their sample distributions in the central aperture exhibit a low likelihood of coming from a common parent distribution. Distributions of their extended aperture exhibit the opposite. This contrast proves the SF differences/similarities along inner/outer extents between merging and isolated objects. In contrast, our H $\alpha$  line emission distributions as function of  $R_e$  (percentage radius/ $R_e$  fractions, see Table 3) suggest that the bigger discrepancies between the control and perturbed samples are found within middle radii (40, 60 and 80%). AD and permutation tests on our EW (H $\alpha$ ) distributions result in likelihoods of practically zero along the annular sequence for all subsamples. In addition, from the KS-Peacock two-sample tests in Table C1, we obtain annular medians per subsample considering only  $D_{2DKS}$  values marked with \*. The resulting trend is similar as that one from Fig. 5, *i.e.* higher values distinguish the central 2D distributions whereas lower, rather constant values characterize the off-central ones.

Furthermore, Moreno *et al.* (2015) use smooth particle hydrodynamics to quantify the induced SF extent in galaxy-pair encounters. The merger phase is ignored due to its complexity. They find that, whenever enhanced SF is triggered in the nucleus, this is always followed by suppression of activity at larger galactocentric radii. We find no evidence of this in our profiles but slight increments in the centres of the perturbed SFG LTS, SFG and all subsamples. Perturbed AGN-like, SFG Red and SFG Green show pronounced enhancements and SFG ETS and SFG Blue seem to show no enhancements at all. Notice that important differences characterize both works. In the sectioning of the radial extension, Moreno *et al.* (2015) use concentric spherical shells of vari-

able widths whereas we use deprojected annuli with widths result of comparing fixed fractions of flux. They also integrate the SFRs all along the interaction time scale whereas we give instantaneous-interacting snapshots. However, our H $\alpha$  line emission distributions (as function of  $R_e$ ) showing the lowest likelihoods of equality within middle radii seem to agree.

Moreno *et al.* (2015) also affirm that the interaction time scale must be long enough for the pair configuration to exhibit both enhancement and suppression. According to their figure 3, suppression disappears for primary galaxies in post-interacting stages (coalescence and post-coalescence) whilst the SF burst remains. To test both, this and the rejuvenation theories, we review the interaction scenarios of perturbed AGN-like galaxies since these are the most favorable ones in the SFR properties. SDSS composed fields containing these galaxies are eye-ball reviewed by two members of the author list. To approximate the role at play (primary or secondary), absolute magnitudes ( $r$  and  $g$  bands) are compared with those of their respective closest companions. After an impartial evaluation of each scenario, we find that perturbed AGN-like galaxies are mostly primaries (33/37) but only four appear actually coalescing and only three have signatures of post-interaction. For primaries in interaction stages, figure 3 of Moreno *et al.* (2015) depicts an enhancement and the slightest suppression. Figures 7 and 8 (AGN-like only) illustrate central suppressions (already catalogued as quenching signatures) and then mostly enhancements.

In general, we find signatures of both central and off-central distinctions and also of rejuvenation within our data.

## 6 SUMMARY AND CONCLUSIONS

By means of the tidal perturbation parameter, CALIFA survey ELGs are sampled into tidally and non-tidally perturbed (control) objects, the former, on a galaxy-pair approach. Ten samples consisting of tidally-perturbed objects match, as proper as possible, the stellar mass and redshift distributions as well as the morphological and photometric properties of the control sample. Even the global source of gas excitation is brought to balance. Powerful tools such as IFS and spectral synthesis of SPs allow us to obtain spatially-resolved properties for the highly-reliable (deprojected) star-forming regions inhabiting these galaxies. Resolved comparisons are conducted at the closest stellar mass densities. Even fairer, AGN-like plus SFG galaxies split up into colours and morphological groups are further distinguished. Several effects on SF consequently emerge:

(i) As distributed on the SFMS plane, most of regions in perturbed galaxies exhibit flatter slopes than those for regions in the control analogues (Fig. 5). Though regions in perturbed objects are indeed older than those in control ones, their offsets with the average SFMS, current-to-past rates and SFR intensities are never inferior (Figs. 7 and 8). Contrasts are favorable indeed for perturbed AGN-like, SFG Red and SFG Green galaxies. For perturbed SFG LTS, SFG and all galaxies, contrasts are also favorable, though only in the centres. Inside-out quenching signatures are found in AGN-like, SFG Red and all subsamples irrespective of either control or perturbed.

(ii) Steeper slopes for regions in perturbed AGN-like, SFG Red and SFG ETS objects do not repeat for regions closest in stellar mass density taken from the rest subsamples (Fig. 9). Dissimilarities in density distributions on the SFMS plane between the former and all types together neither depend nor on the amounts nor on the stellar mass concentration of the regions. Besides, linear fits, either flatter or steeper, do not depend on the stellar mass density of the star-forming regions.

(iii) Regions in perturbed AGN-like galaxies tend to be younger and the differences that advantage them in offset, specific rate and intensity are notable (Figs. 6 to 8). A review of the interaction scenarios of these galaxies suggests that they are mostly primaries, however, their signs of suppressed central SF are related to quenching.

(iv) For perturbed galaxies, weak but detectable correlations result from relating their integrated properties (SFR, its offset and the sSFR) to their tidal perturbation parameters (Fig. 10). We can give just conjectures regarding this weakness that go from depletions of the gas reservoirs to encounters located not at the pericentre. The correlations may explain the typical SFMS flattening that mostly characterizes the regions in these galaxies. Those exceptions might be explained by a dominant stellar mass, so that no local effect is detected. In sum, SF may also depend on the gravitational torques exerted by the closest companions.

(v) On the SFMS plane, slopes for regions combined from control and perturbed galaxies are regularly best represented by the flatter slopes for regions in perturbed galaxies (Table 6). The inclusion of the regions in perturbed objects tends to flatten the SFMS.

On the contrary, Schaefer *et al.* (2019) find tidal interactions neither influencing total sSFRs nor the scale radius of SF relative to the scale radius of the stellar light. However, after discussing all systematics that the estimation of the  $f$  parameter may involve, they do not discard the possibility of tidal interactions enhancing SF in either close pairs or low mass galaxy groups. They propose that either minor mergers or the simple infall of gas from the in-between intergalactic medium are real facts in gas-rich galaxy pairs (Janowiecki *et al.* 2017).

The slight central differences in the SF properties favorable for perturbed galaxies (of SFG LTS, SFG and all types) may reflect contrasts in mass accretion rates (Hall *et al.* 2018). Since their SF suppression is less than that at the centres of control objects (of the same types), tidal perturbations may be driving gas inflows (Moreno *et al.* 2015; Ellison *et al.* 2018b). We intend to confirm this with a forthcoming analysis of oxygen abundances.

## ACKNOWLEDGEMENTS

Authors wish to thank an anonymous Referee for her/his comments and suggestions that improved this work. A. Morales-Vargas thanks Assistant Editor Bella Lock for her kindness.

J. P. Torres-Papaqui and A. Morales-Vargas thank DAIP-UGto for granted support (1006/2016).

S. F. Sánchez thanks CONACyT CB-285080, FC-2016-01-1916 and DGAPA-PAPIIT IN100519 projects for their support.

All figures for this paper were possible by the use of *R: A language and environment for statistical computing*<sup>15</sup>.

The STARLIGHT<sup>16</sup> project is supported by the Brazilian agencies CNPq, CAPES and FAPESP and by the France-Brazil CAPES/Cofecub program.

The SDSS<sup>17</sup> is managed by the Astrophysical Research Consortium for the Participating Institutions: the Brazilian Participation Group, the Carnegie Institution for Science, Carnegie Mellon University, the Chilean Participation Group, the French Participation Group, Harvard-Smithsonian centre for Astrophysics, Instituto de Astrofísica de Canarias, The Johns Hopkins University, Kavli Institute for the Physics and Mathematics of the Universe (IPMU)/University of Tokyo, Lawrence Berkeley National Laboratory, Leibniz Institut für Astrophysik Potsdam (AIP), Max-Planck-Institut für Astronomie (MPIA Heidelberg), Max-Planck-Institut für Astrophysik (MPA Garching), MaxPlanck-Institut für Extraterrestrische Physik (MPE), National Astronomical Observatories of China, New Mexico State University, New York University, Notre Dame University, Observatório Nacional/MCTI, Ohio State University, Pennsylvania State University, Shanghai Astronomical Observatory, United Kingdom Participation Group, Universidad Nacional Autónoma de México, University of Arizona, University of Colorado Boulder, University of Oxford, University of Portsmouth, University of Utah, University of Virginia, University of Washington, University of Wisconsin, Vanderbilt University, and Yale University.

The Calar Alto Legacy Integral Field Area survey is the first legacy survey being performed at Calar Alto and is managed by the CALIFA survey Collaboration<sup>18</sup>. All them would like to thank the IAA-CSIC and MPIA-MPG as major partners of the observatory, and CAHA itself, for the unique access to telescope time and support in manpower and infrastructures. The CALIFA survey Collaboration thanks also the CAHA staff for the dedication to the project.

¡Gracias Mateo!

## DATA AVAILABILITY

The data underlying this article will be shared on reasonable request to the corresponding author.

## REFERENCES

- Abazajian, K. N., Adelman-McCarthy, J. K., *et al.*, 2009, *ApJS* 182, 543
- Aihara, H., Allende Prieto, C., *et al.*, 2011, *ApJS* 193, 29
- Alonso-Herrero, A., Rosales-Ortega, F. F., *et al.*, 2012, *MNRAS* 425, L46
- Argudo-Fernández, M., Shen, S., *et al.*, 2016, *A&A* 592, A30
- Asari, N. V., Cid Fernandes, R., *et al.*, 2007, *MNRAS* 381, 263
- Baldwin, J. A., Phillips, M. M., Terlevich, R., 1981, *PASP* 93, 5
- Barnes, J. E., Hernquist, L. E., 1991, *ApJ* 370, L65
- Barnes, J. E., Hernquist, L. E., 1996, *ApJ* 471, 115
- Barnes, J. E., 2004, *MNRAS* 350, 798
- Barrera-Ballesteros, J. K., Sánchez, S. F., *et al.*, 2015, *A&A* 579, A45
- Beck, S. C., Kovo, O., 1994, in *Mass-Transfer Induced Activity in Galaxies*, ed. Isaac Shlosman, 388
- Bergvall, N., Laurikainen, E., Aalto, S., 2003, *A&A* 405, 31
- Bershady, M. A., Verheijen, M. A. W., 2010, *ApJ* 716, 198
- Bitsakis, T., Charmandaris, V., *et al.*, 2010, *A&A* 517, A75
- Blecha, L., Snyder, G. F., *et al.*, 2018, *MNRAS* 478, 3056
- Brinchmann, J., Charlot, S., *et al.*, 2004, *MNRAS* 351, 1151
- Bruzual, G., Charlot, S., 2003, *MNRAS* 344, 1000
- Byrd, G. G., Valtonen, M. J., *et al.*, 1986, *A&A* 166, 75
- Byrd, G. G., Howard, S., 1992, *AJ* 103, 1089
- Calvi, R., Poggianti, B. M., *et al.*, 2011, *MNRAS* 416, 727
- Cano-Díaz, M., Sánchez, S. F., *et al.*, 2016, *ApJ* 821, L26
- Cano-Díaz, M., Ávila-Reese, V., *et al.*, 2019, *MNRAS* 488, 3929
- Capelo, P. R., Volonteri, M., 2015, *MNRAS* 447, 2123
- Cardelli, J. A., Clayton, G. C. & Mathis, J. S., 1989, *ApJ* 345, 245
- Catalán-Torrecilla, C., Gil de Paz, A., *et al.*, 2015, *A&A* 584, A87
- Catalán-Torrecilla, C., Gil de Paz, A., *et al.*, 2017, *ApJ* 848, 87
- Chabrier, G., 2003, *PASP* 115, 763
- Cicone, C., Maiolino, R., *et al.*, 2014, *A&A* 562 A21
- Cid Fernandes, R., Mateus, A., *et al.*, 2005, *MNRAS* 358, 363
- Cid Fernandes, R., Asari, N. V., *et al.*, 2007, *MNRAS* 375L, 16
- Cid Fernandes, R., Stasińska, G., *et al.*, 2010, *MNRAS* 403, 1036
- Cox, T. J., 2004, in *Star formation and feedback in simulations of interacting galaxies*, PhDT, 27
- Davies, L. J. M., Robotham, A. S. G., *et al.*, 2015, *MNRAS* 452, 616
- Di Matteo, P., Combes, F., *et al.*, 2008, *ASPC* 390, 178
- Elbaz, D., Daddi, E., *et al.*, 2007, *A&A* 468, 33
- Ellison, S. L., Sánchez, S. F., *et al.*, 2018a, *MNRAS* 474, 2039
- Ellison, S. L., Catinella, B., *et al.*, 2018b, *MNRAS* 478, 3447
- Erfanianfar, G., Popesso, P., *et al.*, 2016, *MNRAS* 455, 2839
- Erroz-Ferrer, S., Carollo, C. M., *et al.*, 2019, *MNRAS* 484, 5009
- Fabian, A. C., 2012, *ARA&A* 50, 455
- Falcón-Barroso, J., Sánchez-Blázquez, P., *et al.*, 2011, *A&A* 532, A95
- Freedman Woods, D., Geller, M. J., 2007, *AJ* 134, 527
- García-Benito, R., Zibetti, S., *et al.*, 2015, *A&A* 576, A135
- Gavazzi, G., Fumagalli, M., *et al.*, 2010, *A&A* 517, A73
- Girregularard, D., Thomas, D., *et al.*, 2017, *MNRAS* 465, 688
- Gómez, P. L., Nichol, R. C., *et al.*, 2003, *ApJ* 584, 210
- González Delgado, R. M., García-Benito, R., *et al.*, 2015, arXiv:1506.02809
- González Delgado, R. M., Cid Fernandes, R., *et al.*, 2016, *A&A* 590, A44
- Hall, C., Courteau, S., *et al.*, 2018, *ApJ* 865, 154
- Hernquist, L., Mihos, J. C., 1995, *ApJ* 448, 41

<sup>15</sup> <https://www.R-project.org/>

<sup>16</sup> <http://www.starlight.ufsc.br/>

<sup>17</sup> <http://www.sdss.org/>

<sup>18</sup> <https://bit.ly/2lnB4Um>

- Hopkins, P. F., Hernquist, L., *et al.*, 2008, *ApJS* 175, 356
- Hopkins, P. F., Cox, T. J., *et al.*, 2013, *MNRAS* 430, 1901
- Hsieh, B. C., Lin, L., *et al.*, 2017, *ApJ* 851, L24
- Hummer, D. G., Storey, P. J., 1987, *MNRAS* 224, 801
- Husemann, B., Jahnke, K., *et al.*, 2013, *A&A* 549, A87
- Janowiecki, S., Catinella, B., *et al.*, 2017, *MNRAS* 466, 4795
- Kauffmann, G., Heckman, T., *et al.*, 2003, *MNRAS* 346, 1055
- Kauffmann, G., White, S. D. M., *et al.*, 2004, *MNRAS* 353, 713
- Keenan, R. C., Foucaud, S., *et al.*, 2013, in *IAU Symp. The Intriguing Life of Massive Galaxies*. Ed. D. Thomas, A. Pasquali & I. Ferreras
- Kelz, A., Verheijen, M. A. W., *et al.*, 2006, *PASP* 118, 129
- Kewley, L. J., Dopita, M. A., *et al.*, 2001, *ApJ* 556, 121
- Koyama, S., Koyama, Y., *et al.*, 2019, *ApJ* 874, 142
- Lacerda, E. A. D., Cid Fernandes, R., *et al.*, 2018, *MNRAS* 474, 3727
- Lewis, I., Balogh, M., *et al.*, 2002, *MNRAS* 334, 673
- Li, C. Kauffmann, G., *et al.*, 2008, *MNRAS* 385, 1903
- López-Cobá, C., Sánchez, S. F., *et al.*, 2017, *MNRAS* 467, 4951
- López-Cobá, C., Sánchez, S. F., *et al.*, 2018, *MNRAS* tmp, 2827
- López-Fernández, R., González Delgado, R. M., *et al.*, 2018, arXiv:1802.10118
- Maragkoudakis, A., Zezas, A., *et al.*, 2017, *MNRAS* 466, 1192
- Martig, M., Bournaud, F., *et al.*, 2009, *ApJ* 707, 250
- Martig, M., Croker, A. F., *et al.*, 2013, *MNRAS* 432, 1914
- Mastropietro, C., Moore, B., *et al.*, 2005, *MNRAS* 363, 509
- Mayer, L. Governato, F., *et al.*, 2001, arXiv:astro-ph/9903442
- Medling, A. M., Cortese, L., *et al.*, 2018, *MNRAS* 475, 5194
- Méndez-Abreu, J., Sánchez, S. F., *et al.*, 2019, *MNRAS* 488, L80
- Mihos, J. C., Richstone, D. O., Bothun, G. D., 1992, *ApJ* 400, 153
- Mihos, J. C., Hernquist, L., 1994, *ApJL* 431, L9
- Mihos, J. C., Hernquist, L., 1996, *ApJ* 464, 641
- Moreno, J., Torrey, P., *et al.*, 2015, *MNRAS* 448, 1107
- Peacock, J. A., 1983, *MNRAS* 202, 615
- Peng, Y.-j., Lilly, S. J., *et al.*, 2010, *ApJ* 721, 193
- Perez, M. J., Tissera, P. B., *et al.*, 2005, arXiv:0510327
- Renzini, A., Peng, Y.-j., 2015, *ApJ* 801, L29
- Rosales-Ortega, F. F., Kennicutt, R. C., *et al.*, 2010, *MNRAS* 405, 735
- Roth, M. M., Kelz, A., *et al.*, 2005, *PASP* 117, 620
- Salim, S., Rich, R. M., *et al.*, 2007, *ApJS* 173, 267
- Sánchez-Blázquez, P., Peletier, R. F., *et al.*, 2006, *MNRAS* 371, 703
- Sánchez, S. F., Kennicutt, R. C., *et al.*, 2012a, *A&A* 538, A8
- Sánchez, S. F., Rosales-Ortega, F. F., *et al.*, 2013, *A&A* 554, A58
- Sánchez, S. F., Rosales-Ortega, F. F., *et al.*, 2014, *A&A* 563, A49
- Sánchez, S. F., García-Benito, R., *et al.*, 2016a, *A&A* 594, A36
- Sánchez, S. F., Avila-Reese, V., *et al.*, 2018a, arXiv:1807.11528
- Sánchez, S. F., Avila-Reese, V., *et al.*, 2018b, *RMxAA* 54, 217
- Schaefer, A. L., Croom, S. M., *et al.*, 2017, *MNRAS* 464, 121
- Schaefer, A. L., Croom, S. M., *et al.*, 2019, *MNRAS* 483, 2851
- Schawinski, K., Thomas, D., *et al.*, 2007, *MNRAS* 382, 1415
- Schawinski, K., Urry, C. M., *et al.*, 2014, *MNRAS* 440, 889
- Schiminovich, D., Wyder, T. K., *et al.*, 2007, *ApJS* 173, 315
- Speagle, J. S., Steinhardt, C. L., *et al.*, 2014, *ApJS* 214, 15
- Springel, V., 2000, *MNRAS* 312, 859
- Springel, V., Di Matteo, T., Hernquist, L., 2005, *MNRAS* 361, 776
- Tissera, P. B., Domínguez-Tenreiro, R., *et al.*, 2002, *MNRAS* 333, 327
- Torres-Papaqui, J. P., Coziol, R., *et al.*, 2012a, *ApJ* 754, 144
- Torres-Papaqui, J. P., Coziol, R., *et al.*, 2012b, *RMxAA* 48, 275
- Varela, J., Moles, M., *et al.*, 2004, *A&A* 420, 873
- Ventou, E., Contini, T., *et al.*, 2019, arXiv:1909.03706
- Violino, G., Ellison, S. L., *et al.*, 2018, *MNRAS* 476, 2591
- Vulcani, B., Poggianti, B. M., *et al.*, 2015, *ApJ* 798, 52
- Vulcani, B., Poggianti, B. M., *et al.*, 2019, *MNRAS* 480, 3152
- Walcher, C. J., Wisotzki, L., *et al.*, 2014, *A&A* 569, A1
- Wild, V., Rosales-Ortega, F. F., *et al.*, 2014, *A&A* 567, A132
- Whitaker, K. E., van Dokkum, P. G., *et al.*, 2012, *ApJ* 754, L29
- Yan-Chun, S., Xu, C. K., *et al.*, 2003, *ChPhL* 20, 1652
- Young, J. S., 1999, *IAUS* 186, 217
- Yuan, F.-t., Takeuchi, T. T., *et al.*, 2012, *A&A* 548, A117
- Yuanhui, X., 2017, in *A fast algorithm for two-dimensional Kolmogorov-Smirnov two-sample tests*, *Computational Statistics & Data Analysis*, Elsevier, vol. 105, p. 53-58.
- Zheng, Z., Wang, H., *et al.*, 2017, *MNRAS* 465, 4572

This paper has been typeset from a  $\text{\TeX}/\text{\LaTeX}$  file prepared by the author.

## APPENDIX A: THE TIDALLY-PERTURBED SAMPLES

Fundamental and other properties for control and perturbed objects (see Table A1). The latter are the closest, in the five fundamentals ( $M_*$ ,  $z$ , morphological group, galaxy colour and dominant excitation source), to each single control object.









Table A1: Fundamental properties for control ( $f < -4.5$ ) and perturbed ( $f \geq -4.5$ ) objects. Some other properties are also listed.

NED name	Global $M_*$ $\log_{10}$ ( $M_\odot$ ) <sup>a</sup>	$z$ <sup>b</sup>	Morphology (Collaboration) <sup>c</sup>	Morphological group <sup>d</sup>	Galaxy colour type <sup>e</sup>	Dominant excitation source (BPT) <sup>f</sup>	Surface scale (kpc <sup>2</sup> ) <sup>g</sup>	Axis ratio <sup>h</sup>	$f$ parameter. <sup>i</sup>	Deprojection. <sup>j</sup>	H $\alpha$ flux 60 % radius / $R_e$ <sup>k</sup>	Median SP age $\log_{10}$ (yr) <sup>l</sup>	Number of star-forming regions <sup>m</sup>	Global SFR $\log_{10}$ ( $M_\odot \text{ yr}^{-1}$ ) <sup>n</sup>
UGC05358	9.27	0.00968	SdB(N)	LTS	blue	SFG	0.0382	0.33	-2.698	y	0.98	9.53	352	-0.7942
NGC5714	10.02	0.00757	SbA(N)	ETS	green	SFG	0.0234	0.13	-2.693	Y	1.10	9.93	756	-0.3268
UGC01123	10.55	0.01627	SabA(N)	ETS	red	TO	0.1079	0.31	-2.643	N	1.90	9.92	7	-2.2320
UGC05244	9.44	0.00999	SbcA(N)	LTS	blue	LINER	0.0407	0.22	-2.637	N	0.56	9.67	495	-0.5615
UGC02690	9.82	0.02090	ScdAB(N)	LTS	blue	SFG	0.1780	0.40	-2.634	Y	1.74	9.63	484	0.3788
NGC0941	9.39	0.00555	ScdA(N)	LTS	blue	SFG	0.0126	0.87	-2.614	Y	0.83	9.60	2104	-0.6081
NGC7819	10.19	0.01660	SbA(N)	LTS	blue	SFG	0.1123	0.53	-2.568	Y	0.93	9.71	656	0.2006
NGC7321	11.07	0.02371	SbcB(N)	LTS	green	TO	0.2291	0.69	-2.555	Y	1.04	9.70	774	0.5092
UGC05598	10.21	0.01883	SbA(N)	ETS	green	SFG	0.1445	0.30	-2.545	Y	0.85	9.77	410	0.1507
UGC05396	10.21	0.01798	SbcAB(N)	LTS	green	SFG	0.1317	0.27	-2.503	Y	0.88	9.74	287	-0.3202
UGC08781	11.08	0.02513	SbB(N)	ETS	red	SFG	0.2573	0.52	-2.419	Y	1.94	9.94	8	-1.9950
UGC05108	10.97	0.02711	SbB(N)	ETS	red	SFG	0.2995	0.77	-2.419	Y	1.07	9.84	85	-0.4272
UGC09165	10.63	0.01772	SaA(N)	ETS	red	SFG	0.1280	0.24	-2.416	N	0.54	9.89	127	0.4543
NGC0192	10.83	0.01386	SabA(N)	ETS	red	SFG	0.0783	0.31	-2.347	Y	0.85	9.94	115	-0.1839
NGC7591	10.82	0.01634	SbcB(N)	LTS	red	SFG	0.1088	0.59	-2.296	Y	0.72	9.78	443	0.5792
UGC02319	10.46	0.02344	SbcA(N)	LTS	red	SFG	0.2238	0.25	-2.270	Y	0.97	9.79	155	-0.3660
NGC0001	10.77	0.01511	SbcA(N)	LTS	green	TO	0.0930	0.80	-2.252	Y	0.76	9.91	478	0.6000
NGC5730	9.80	0.00853	ScdA(N)	LTS	green	SFG	0.0296	0.20	-2.250	Y	1.19	9.86	1082	-0.2019
NGC2449	10.77	0.01652	SabAB(N)	ETS	red	SFG	0.1112	0.50	-2.181	Y	0.94	9.93	62	-0.7484
NGC0444	9.85	0.01605	ScdA(N)	LTS	blue	TO	0.1050	0.24	-2.150	N	0.69	9.61	587	-0.2877
NGC0496	10.41	0.02005	ScdA(N)	LTS	green	TO	0.1639	0.58	-2.147	Y	0.91	9.74	919	0.4443
UGC09873	9.99	0.01867	SbA(N)	ETS	green	SFG	0.1420	0.21	-2.069	Y	0.93	9.74	324	-0.0757
NGC5480	9.99	0.00641	ScdA(N)	LTS	blue	SFG	0.0167	0.67	-2.040	Y	1.19	9.53	1744	0.1900
UGC09665	10.03	0.00843	SbA(N)	ETS	green	SFG	0.0290	0.23	-1.976	N	0.78	9.83	749	0.0248
NGC5379	9.69	0.00599	SabAB(N)	ETS	green	SFG	0.0146	0.37	-1.950	Y	0.41	10.07	60	-1.4878
NGC0477	10.57	0.01963	SbcAB(N)	LTS	green	SFG	0.1570	0.66	-1.832	Y	0.72	9.79	653	0.1941
NGC1094	10.72	0.02150	SbAB(N)	ETS	green	SFG	0.1884	0.71	-1.689	Y	1.13	9.48	592	0.4774
NGC3994	10.57	0.01036	SbcAB(N)	LTS	green	SFG	0.0438	0.47	-1.602	Y	0.64	9.50	412	0.4170
NGC0036	11.02	0.01992	SbB(N)	ETS	red	SFG	0.1617	0.65	-1.584	Y	0.72	9.83	157	-0.2341
NGC5000	10.64	0.01864	SbcB(N)	LTS	green	SFG	0.1415	0.60	-1.581	Y	1.10	9.91	121	-0.2875
NGC5425	9.63	0.00702	ScdAB(N)	LTS	blue	SFG	0.0201	0.27	-1.468	N	1.53	9.84	1044	-0.5270
UGC00312	10.25	0.01449	SdB(N)	LTS	blue	SFG	0.0856	0.35	-1.371	Y	1.25	9.71	1529	0.5029
UGC09080	9.24	0.01019	ScA(N)	LTS	blue	SFG	0.0423	0.14	-1.366	N	1.35	9.67	360	-0.6498
NGC2604	9.77	0.00707	SdB(N)	LTS	blue	SFG	0.0204	0.88	-1.354	Y	0.82	9.38	2143	-0.1008
NGC3991	10.17	0.01076	SmA(N)	LTS	blue	SFG	0.0472	0.22	-1.325	N	0.43	9.43	1110	0.4420
NGC5829	9.84	0.01873	ScA(N)	LTS	blue	TO	0.1430	0.76	-1.243	Y	1.12	9.48	300	-0.2554
UGC08733	9.27	0.00779	SdmB(N)	LTS	green	SFG	0.0249	0.49	-1.202	Y	1.04	9.33	757	-0.7846
UGC12494	9.49	0.01622	SdB(N)	LTS	blue	TO	0.1072	0.35	-0.978	Y	1.45	9.67	456	-0.3431
UGC12688	10.08	0.01740	ScdAB(Y)	LTS	green	SFG	0.1234	0.29	-0.975	Y	1.24	9.42	594	0.3194
UGC10331	10.08	0.01517	ScAB(Y)	LTS	blue	SFG	0.0938	0.26	-0.946	N	0.50	9.73	808	0.2916
NGC5320	10.18	0.00882	SbcAB(N)	LTS	blue	SFG	0.0317	0.55	-0.806	Y	0.87	9.61	1785	-0.2310
UGC04210	9.88	0.01678	ScdA(N)	LTS	green	SFG	0.1147	0.23	-0.292	Y	1.15	9.78	284	-0.2391
NGC5951	9.53	0.00622	ScdAB(N)	LTS	blue	SFG	0.0158	0.22	-0.274	Y	0.53	9.65	1108	-0.5091
VV488NED02	10.45	0.01648	SbAB(Y)	ETS	red	SFG	0.1095	0.18	-0.226	N	0.62	9.93	314	0.0229
UGC09476	10.07	0.01079	SbcA(N)	LTS	blue	SFG	0.0474	0.63	-0.178	Y	1.18	9.58	1300	-0.0202
NGC7549	10.41	0.01546	SbcB(N)	LTS	red	SFG	0.0993	0.75	-0.057	Y	0.60	9.57	383	0.4454
UGC04722	8.45	0.00593	SdmA(N)	LTS	blue	SFG	0.0143	0.19	0.313	N	0.44	8.54	268	-1.2170
NGC0523	10.73	0.01573	SdAB(Y)	LTS	red	SFG	0.0449	0.24	0.669	Y	1.76	9.42	458	0.1845
NGC3395	9.70	0.00533	ScdAB(Y)	LTS	blue	SFG	0.0116	0.53	1.027	Y	0.78	9.13	2557	-0.0233

<sup>a</sup> Global stellar mass (see Section 2.3.2).<sup>b</sup> Raw redshift measured from the CALIFA cube.<sup>c</sup> Reclassification of morphologies (see Section 2.2).<sup>d</sup> Sbc and later types as Late Type Spirals (LTSs). All the rest as Early Type Spirals (ETs) (which include a few Early Types, ETs).<sup>e</sup> CMD (see Section 2.2 and Fig. 3).<sup>f</sup>  $[\text{O III}]/\text{H}\beta$  against  $[\text{N II}]/\text{H}\alpha$  (BPT diagnostic diagram, Baldwin, Phillips & Terlevich 1981).<sup>g</sup> Equivalence of 1 arcsec<sup>2</sup>.<sup>h</sup> Semiminor to semimajor axis ratio from light moment analyses (see W-14). Also  $\cos\phi$ , *i.e.*, the cosine of the inclination angle (see Fig. 1).<sup>i</sup> Tidal perturbation parameter (see Section 3.1).<sup>j</sup> Deprojection: Yes (Y), no (N). Relocation of each spaxel coordinates on a disk plane.<sup>k</sup> H $\alpha$  emission distribution: radius containing 60% of the H $\alpha$  flux as a function of  $R_e$  (see Section 3.5).<sup>l</sup> Median SP age (see Section 2.3.2).<sup>m</sup> Number of star-forming regions (see Section 2.3.1).<sup>n</sup> Global SFR (see Section 2.3.1).

**APPENDIX B: AN IMPORTANT NOTE ON THE ANNULAR PROFILES**

To minimize the influence of stellar mass, in each annular set of spaxel properties, the perturbed spaxels from each trial (tA to tJ, see Section 3.3) are paired with control ones by minimizing their differences in  $\Sigma_*$ . The medians of these annular differences are plotted as the  $\Sigma_*$  profiles of Fig. B1. All profiles of Section 4 plot each annular difference of the respective property in the same way as the median differences of Fig. B1. Notice, for the  $\Sigma_*$ , that control and perturbed sample profiles overlap since all bar heights are  $\sim 0$  dex (rounded numbers at two figures). Besides, from comparing each annular distribution pair, an important fraction of the AD-permutation tests gives high likelihoods. Cases in which at least one likelihood (either AD or permutation) does not reach the half are identified in Figs. B1 and B2. The reason why is the unbalance in the number of spaxels or star-forming regions to be paired (see Section 3.4). Such unbalances reduce the probability of finding the best minimum absolute difference between paired spaxels. To review this issue, we further show the involved distributions and perform on them the Mann-Whitney (MW) test. The null hypothesis of this test is that the distributions to be compared differ by a location shift (mainly the median). Notice that the third numbers, *i.e.* the MW *p*-values in the identified cases (AGN-like, SFG Red and SFG ETS panels of Fig. B1), are much greater than the statistical level so the null hypothesis is rejected. Moreover, by looking at the distributions of Fig. B2, the only dissimilar ones are those for the central annulus. As suggested by the MW test, the medians and also the IQRs are alike except the distribution tails, specifically, those of the control sample (20% annulus). In sum, results for the centres of AGN-like, SFG Red and SFG ETS galaxies are the only ones that must be taken with care (both AD and permutation tests do not suggest similitude).

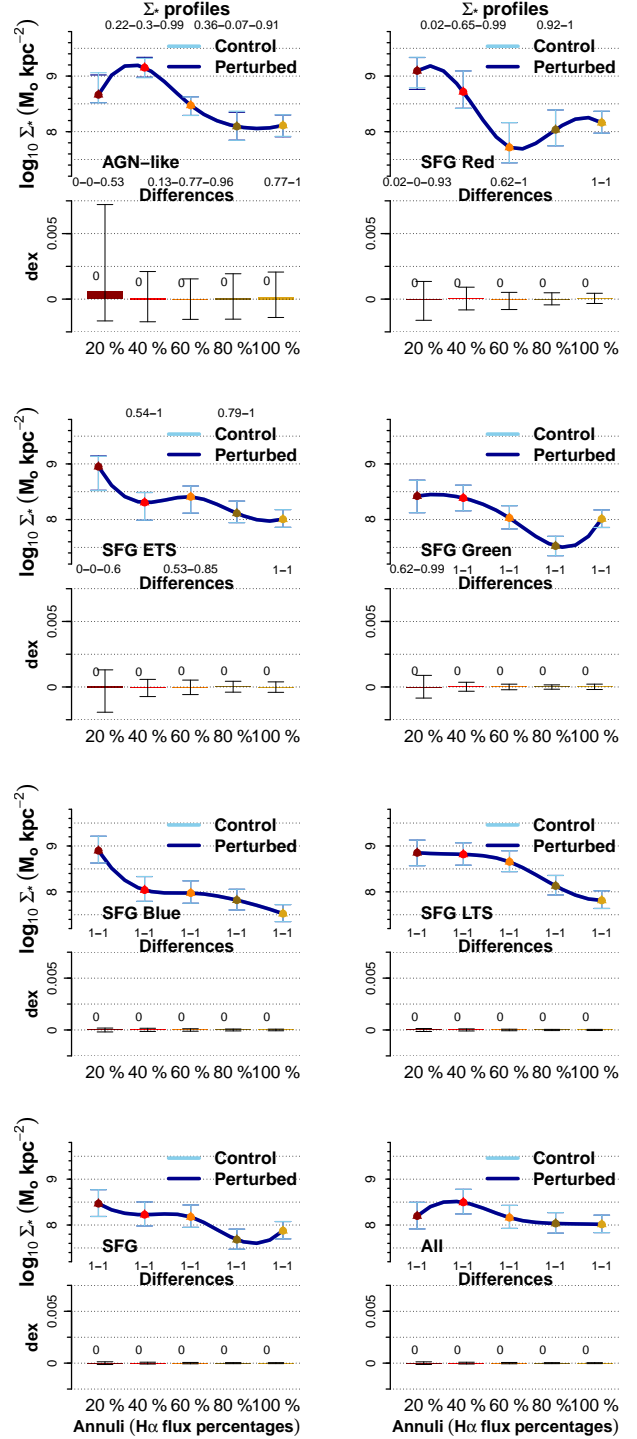


**Figure B1.** Annular profiles:  $\Sigma_*$ . Throughout this work, all profiles use the amounts of annular star-forming regions per sample and subsample as in Fig. 5. Five consecutive-outward annuli denote the radial extension (see Section 3.5). “Differences” (bar heights by always subtracting the control values from the perturbed ones) are the medians of the annular distributions of differences (differences by pairing sample spaxels which are the closest in  $\Sigma_*$ ). Bar lines depict the interquartile ranges (IQRs, 1st to 3rd) of the distributions of differences. Symbols are both sample values giving each Difference. Symbol lines depict the IQRs of the annular distributions of each sample. Above and below the profiles, likelihoods from AD-permutation tests are found for each pair of sample distributions. Finally, a third statistics, Mann-Whitney (MW) test *p*-value, is given when at least one of the other two statistics results in a value lower than 0.5 (see text).

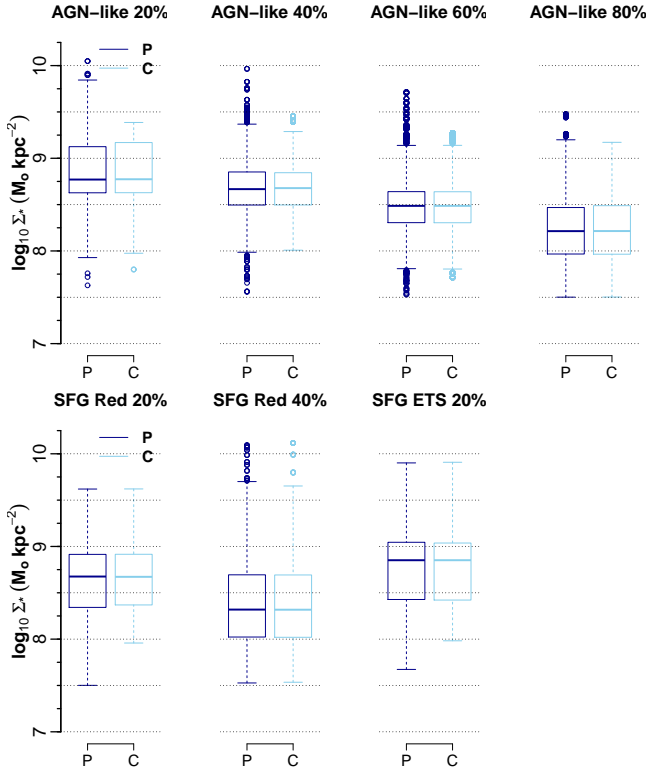


**Figure B2.**  $\Sigma_*$  distributions (P, perturbed, against C, control) for the annular cases of Fig. B1 in which at least one of the statistical tests results in a likelihood lower than 0.5.

### APPENDIX C: RESOLVED SFMS

The annular comparison sets are shown in Table C1. It lists the linear regression coefficients of control and tA to tJ samples all on the SFMS plane. In each set, slopes marked with \* are the closest ones to the slopes which result from the data in the respective set. Only significance difference tests (SDTs, see Section 4.1) with values above the statistical level are considered for this and that slope with the highest test value is marked (see Section 5.4). The criterion is that slopes are suggested to be different when the SDT value falls below the statistical level. Only these cases of different slopes are considered for comparisons (see Section 4.1). At last, from the K-S/Peacock two-sample test,  $D_{2DKS}$  differences marked with \* reject the null hypothesis of a parent distribution as the origin.







